Article

Cell Chemical Biology

Natural products chlorotonils exert a complex antibacterial mechanism and address multiple targets

Graphical abstract

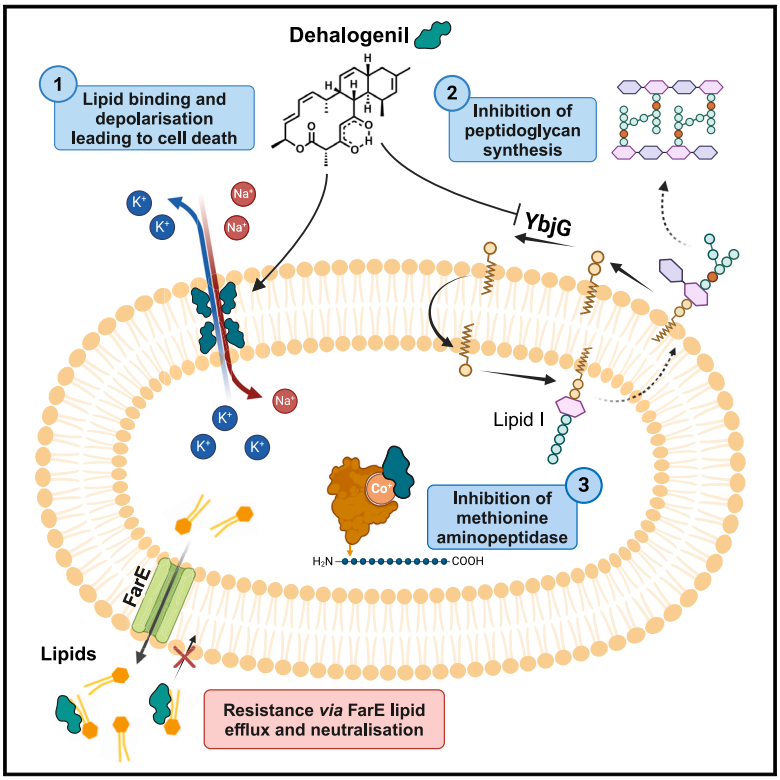

Highlights

- Natural products chlorotonils are fast-acting, non-lytic, and target the membrane
- Chlorotonils bind to lipids and induce membrane depolarization by potassium efflux
- YbjG (peptidoglycan synthesis) and MetAP (protein synthesis) are secondary targets
- The optimized lead structure dehalogenil is safe in mouse models

Authors

Felix Deschner, Dietrich Mostert, Jan-Martin Daniel, ..., Stephan Sieber, Rolf Müller, Jennifer Herrmann

Correspondence

jennifer.herrmann@helmholtz-hips.de

In brief

New antibiotics are urgently needed to tackle the global antimicrobial resistance crisis. Deschner et al. characterized Dehalogenil, a fast-acting natural product derivative, and found that it combines a complex mechanism of action with resistance-breaking properties and good safety in mouse models.

Deschner et al., 2025, Cell Chemical Biology *32*, 586–602
April 17, 2025
https://doi.org/10.1016/j.chembiol.2025.03.005

CellPress

CellPress
OPEN ACCESS

Cell Chemical Biology

Article

Natural products chlorotonils exert a complex antibacterial mechanism and address multiple targets

Felix Deschner,[1,2,3,4] Dietrich Mostert,[5] Jan-Martin Daniel,[4,6] Alexander Voltz,[1,2,3,4] Dana Carina Schneider,[4,7] Navid Khangholi,[8] Jürgen Bartel,[9] Laís Pessanha de Carvalho,[10] Madita Brauer,[11] Tatiana E. Gorelik,[1,2,12,16] Christian Kleeberg,[13] Timo Risch,[1,2,3,4] F.P. Jake Haeckl,[1,2,4] Laura Herraiz Benítez,[1,2] Anastasia Andreas,[1,2,4] Andreas Martin Kany,[1,2,3,4] Gwenaëlle Jézéquel,[1,2,4] Walter Hofer,[1,2,4] Mathias Müsken,[2] Jana Held,[4,10] Markus Bischoff,[2,14] Ralf Seemann,[7] Heike Brötz-Oesterhelt,[4,7,15] Tanja Schneider,[4,6] Stephan Sieber,[1,5] Rolf Müller,[1,2,3,4] and Jennifer Herrmann[1,2,3,4,17,*]

[1]Microbial Natural Products, Helmholtz Institute for Pharmaceutical Research Saarland (HIPS), 66123 Saarbrücken, Germany
[2]Helmholtz Centre for Infection Research (HZI), 38124 Braunschweig, Germany
[3]Department of Pharmacy, Saarland University, 66123 Saarbrücken, Germany
[4]German Centre for Infection Research (DZIF), partner sites: Bonn-Cologne, Hannover-Braunschweig, and Tübingen, 38124 Braunschweig, Germany
[5]Center for Functional Protein Assemblies, TUM School of Natural Sciences, Technical University of Munich, 85748 Garching, Germany
[6]Institute for Pharmaceutical Microbiology, University of Bonn, University Hospital Bonn, 53127 Bonn, Germany
[7]Interfaculty Institute of Microbiology and Infection Medicine Tübingen, Department of Microbial Bioactive Compounds, University of Tübingen, 72074 Tübingen, Germany
[8]Experimental Physics and Center for Biophysics, Saarland University, 66123 Saarbrücken, Germany
[9]Department of Microbial Proteomics, Institute of Microbiology, University of Greifswald, 17489 Greifswald, Germany
[10]Institute of Tropical Medicine, Eberhard Karls University Tübingen, 72074 Tübingen, Germany
[11]Department of Microbial Physiology and Molecular Biology, Institute of Microbiology, University of Greifswald, 17489 Greifswald, Germany
[12]Institute of Inorganic and Analytical Chemistry, Goethe University Frankfurt, 60438 Frankfurt am Main, Germany
[13]Institute for Inorganic and Analytical Chemistry, Technical University of Braunschweig, 38106 Braunschweig, Germany
[14]Institute for Medical Microbiology and Hygiene, Saarland University, 66421 Homburg, Germany
[15]Cluster or Excellence "Controlling Microbes to Fight Infections", Tübingen, Germany
[16]Ernst Ruska-Centre for Microscopy and Spectroscopy with Electrons, Forschungszentrum Jülich GmbH, Jülich 52428, Germany
[17]Lead contact
*Correspondence: jennifer.herrmann@helmholtz-hips.de
https://doi.org/10.1016/j.chembiol.2025.03.005

SIGNIFICANCE The WHO urgently calls for the development of new antibacterial agents that can overcome existing resistance in critical human pathogens. Chlorotonils target such high-priority organisms and, as we show here, combine a unique mechanism of action with resistance-breaking properties making them promising candidates for clinical development.

SUMMARY

Antimicrobial resistance is a threat to human health rendering current first-line antibiotics ineffective. New agents overcoming resistance mechanisms are urgently needed to guarantee successful treatment of human disease in the future. Chlorotonils, a natural product class with yet unknown mode of action, were shown to have broad-spectrum activity against multi-resistant Gram-positive bacteria and the malaria parasite *Plasmodium falciparum,* with promising activity and safety in murine infection models. Here, we report that chlorotonils can target the cell membrane, cell wall, and protein biosynthesis. They can be characterized by a rapid onset of action via interference with ion homeostasis leading to membrane depolarization, however, without inducing severe barrier failure or cellular lysis. Further characterization confirmed binding of chlorotonils to bacterial membrane lipids eventually leading to uncontrolled potassium transport. Additionally, we identified functional inhibition of the peptidoglycan biosynthesis protein YbjG and methionine aminopeptidase MetAP as secondary targets of chlorotonils.

INTRODUCTION

Antimicrobial resistance (AMR) is a major threat to human health and was directly responsible for 1.27 million deaths globally in 2019.[1] The numbers are expected to increase to up to 10 million annual deaths by 2050 with significant consequences for world economics with losses in the range of up to $4 trillion (3.8% of global gross domestic product).[2] By now, bacterial resistance mechanisms against all antibiotics on the market are reported, posing significant challenges for clinical treatment; hence, antibiotics with novel modes of action – able to overcome and prevent AMR – are urgently needed. Unfortunately, the antibiotic pipeline is almost dry and the approval of new classes of antibiotics is challenging, as research bears significant scientific and economic challenges.[3–5] In the last decade, only 19 small molecule antibacterials have been approved, and none of them as a member of a new class.[6] In 2017, the World Health Organization released a list of priority pathogens with a recent update in 2024, specifically calling for new treatment options for infections caused by several Gram-negative bacteria and multi-resistant Gram-positive species such as vancomycin-resistant *Enterococcus faecium* (VRE) or methicillin-resistant *Staphylococcus aureus* (MRSA).[7,8]

Natural products continue to be a major source of new antimicrobial drugs.[9] Chlorotonils are macrocyclic antibiotics originally isolated from the myxobacterium *Sorangium cellulosum* with excellent activity against multidrug-resistant human pathogens like VRE and MRSA, and the malaria-causing parasite *Plasmodium falciparum*.[10] We have previously published semi-synthetic approaches to produce our first- and second-generation frontrunner molecules ChB1-Epo2 and dehalogenil (DHG), respectively, starting from the main fermentation product chlorotonil A (ChA) (Figure S1).[11,12] DHG is characterized by improved physicochemical properties, a better toxicological profile as well as prominent *in vivo* activity in mouse models of *S. aureus* infection.[12] Recently, we have reported on potential interference with ion homeostasis in *Clostridioides* (previously *Clostridium*) *difficile*, outgrowth-inhibition of *C. difficile* endospores, and microbiota-sparing effects in a mouse infection model.[13] For anthracimycin, an antibiotic structurally similar to chlorotonil, DNA and RNA synthesis were proposed as potential target areas.[14–16] However, a defined target structure has not yet been identified so far.

We provide here a concise evaluation of the mode of action (MoA) of this new class of antimicrobial natural products. We report the identification of lipid-targeted membrane depolarization causing uncontrolled potassium efflux as primary antibacterial mechanism of chlorotonils, in combination with functional inhibition of both, the membrane-bound phosphatase YbjG and the cytoplasmic methionine aminopeptidase MetAP. Based on this unique MoA, chlorotonils are promising candidates for antibiotic drug development since they overcome existing resistance mechanisms and do not promote a rapid development of resistance.

RESULTS

Chlorotonils are fast-acting but do not cause severe membrane-barrier failure

We performed susceptibility assays and assessed potential lytic behavior of the compound class to initially characterize its antibacterial effects. We found that DHG is highly active against *S. aureus* ATCC29213 (minimum inhibitory concentration MIC = 31.25 ng/mL). Notably, inhibitory activity was evident at concentrations far below the MIC recorded after 24h co-incubation (Figure 1A), with significantly delayed maximum growth rate at concentrations as low as 2 ng/mL (0.0625-fold MIC, Figure 1B). At even lower concentrations (0.5 ng/mL, 0.0156-fold MIC), we observed a significant effect on the maximal growth rate (Figure 1C). Once cells started to grow, there were no significant differences in growth rates of cells treated with 0.25- to 0.0313-fold MIC (Figure 1C). The addition of DHG to *S. aureus* cells in early exponential phase did not reveal any lytic effects, but showed immediate growth inhibition, while 10 μM melittin lysed cells completely within 1 h (Figure 1D).

We have previously published chlorotonils as active against Gram-positive bacteria.[11] We reevaluated this statement using non-typical Gram-positive *Mycobacterium tuberculosis* H37Ra and an *E. coli* strain lacking TolC (Δ*tolC*) co-treated with sub-inhibitory concentrations of polymyxin B nonapeptide (PMBN). We demonstrated chlorotonil activity against both *mycobacteria* and PMBN-treated *E. coli* ΔtolC (Figure 1E) confirming presence of the target in these bacteria, which has implications on subsequent MoA studies.

Understanding kinetics is also crucial for MoA studies. Thus, *S. aureus* ATCC29213 was exposed to DHG and samples were taken at different time points to determine viable cell counts (Figure 1F). This unveiled a rapid onset of action for DHG: after only a few minutes of treatment at supra-MIC, no colony-forming units (CFUs) were observed, suggesting a bactericidal MoA (>3-$\log_{10}$ reduction) likely acting on the bacterial cell envelope given the extremely fast onset of activity. Sub-MIC (0.5-fold), DHG initially caused a 3-log reduction in CFU, but cells recovered approximately 3h after treatment. Regrowth was not due to spontaneous resistance, as isolated clones showed no change in susceptibility (not shown).

We then applied scanning/transmission electron microscopy (SEM, TEM) to check for obvious cell damages (Figure 1G). EM images confirmed the presence of intact *S. aureus* cells even after 1h DHG treatment at 10-fold MIC, with membrane integrity seemingly intact; however, treated cells appeared to carry membrane invaginations (Figure 1G) further underlining the hypothesis of a membrane-directed MoA. To check for membrane pores, we performed a SYTO9/propidium iodide (PI) staining (Figure 1H) using *S. aureus*. Cells remained PI-negative (green) even after 1h treatment at 10-fold MIC, indicating the presence of an intact membrane (no large pore formation). Visualizing the impact of DHG on the cytoplasmic membrane, we switched to *Bacillus subtilis* 168 as indicator strain for staining with the lipid dye FM5-95 (Figure 1I). Again, cells treated with 10-fold MIC for 1h did not show any differences to control cells. However, after prolonged treatment (4h), we could observe an increased size of several *Bacillus* cells (25%, Figure S2A), suggesting impaired structural rigidity and an affected cell wall. Using identical conditions, *S. aureus* cell size increased by 30% (Figure S2B).

Dehalogenil affects peptidoglycan synthesis by binding to the phosphatase YbjG

As the unusual morphology of DHG-treated cells (Figure 1I) suggested a weakened cell wall, we checked for cell envelope stress

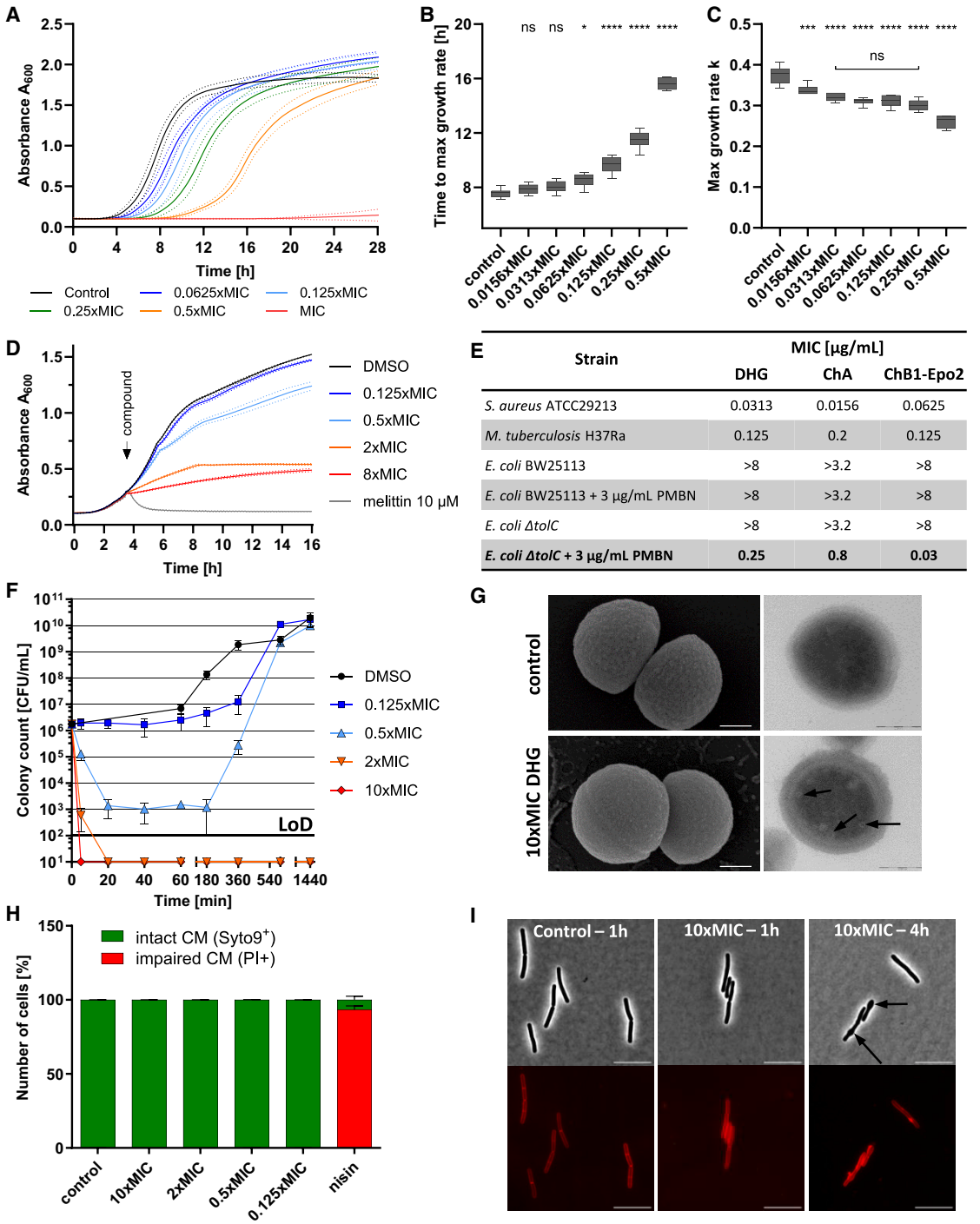

Strain	MIC [µg/mL]		
	DHG	ChA	ChB1-Epo2
S. aureus ATCC29213	0.0313	0.0156	0.0625
M. tuberculosis H37Ra	0.125	0.2	0.125
E. coli BW25113	>8	>3.2	>8
E. coli BW25113 + 3 µg/mL PMBN	>8	>3.2	>8
E. coli ΔtolC	>8	>3.2	>8
***E. coli ΔtolC* + 3 µg/mL PMBN**	**0.25**	**0.8**	**0.03**

Figure 1. Chlorotonils are fast-acting but do not cause severe membrane-barrier failure

(A) Susceptibility assay shows significant sub-MIC activity of DHG against *S. aureus* ATCC29213, with the corresponding time to max. growth rate and max. growth rate (B and C). Mean and SD are shown (n = 6) and compared using one-way ANOVA.

(D) Lysis assay utilizing *S. aureus* does not show immediate lysis of DHG. Melittin (10 µM) was used as control.

(E) Chlorotonils exert activity against *M. tuberculosis* and efflux-deficient *E. coli* (*ΔtolC*) when used alongside with polymyxin nonapeptide (PMBN) treatment to further weaken the outer membrane.

(F) Time-kill curve of DHG against *S. aureus* (n = 3), with a limit of detection at 100 CFU/mL and mean with SD shown.

(G) Scanning and transmission electron microscopy images of *S. aureus* treated with DMSO or DHG for 1h. Arrows indicate membrane invaginations. Scale 200 nm.

(legend continued on next page)

and potential inhibition of major steps in peptidoglycan synthesis (Figure 2A).

In *B. subtilis*, the *lial* promotor was mildly induced at 1-fold MIC for 3h (Figure 2B), indicative of interference with the undecaprenyl cycle in cell wall synthesis,[17] while all other reporters did not show any response (not shown). The accumulation of the UDP-MurNAc pentapeptide can be used to pinpoint to a membrane-associated step of cell wall synthesis.[18] Indeed, we detected a mild accumulation of UDP-MurNAc pentapeptide in *S. aureus* following DHG treatment (Figure 2C), with up to 300% increase at 5-fold MIC compared to untreated cells. Ensuing, we checked if DHG has a direct influence on peptidoglycan synthesis proteins, and could confirm dose-dependent inhibition of YbjG (IC_{50} = 32.5 ng/mL; 0.079 μM) (Figures 2D and 2E), while MraY, MurG, and PBP2-catalysed reactions were unaffected (not shown). Inhibition of the membrane-bound phosphatase YbjG prevents recycling of the lipid carrier undecaprenyl-pyrophosphate (C55-PP) to undecaprenyl-phosphate (C55-P).[19] Using microscale thermophoresis (MST), direct binding of DHG to YbjG was confirmed (K_D = 5.75 ± 0.57 μM) (Figure 2F). Limited aqueous solubility of DHG prevented complete saturation of the protein in the MST assay. While YbjG inhibition likely contributes to the chlorotonil MoA and the observed swelling of DHG-treated cells, the rapid kill-kinetic cannot be solely attributed to the inhibition the C55-P recycling process, especially because YbjG function is redundant to some extent.[19,20]

Activity of chlorotonils is primarily mediated by membrane depolarization

Instead of severe membrane barrier failure, we hypothesized that a non-lytic activity, characterized by a rapid onset of action could be attributed to membrane depolarization effects. To test this, we used a Nernstian dye ($DiOC_2(3)$), which after incorporation into the membrane emits red fluorescence. Release from the membrane (during depolarization) then causes a shift to green fluorescence; hence, the ratio of red/green fluorescence can be used as measure of membrane potential (V_m). The protonophore CCCP (5 μM) served as positive control.

We detected changes in membrane potential (V_m) in *S. aureus* cells treated with DHG at a concentration as low as 2–4 ng/mL (Figure 3A). The extent of depolarization became more pronounced with increasing DHG concentrations, reaching its peak at 4- to 8-fold the MIC at an app. 40% V_m level compared to the DMSO control. The depolarization observed was neither as rapid nor as extensive as induced by 5 μM CCCP (15% V_m level compared to control); for 1000 ng/mL DHG, the rate constant k (1/min) was found to be 0.15, whereas for CCCP k was 0.38 (Table SI1). Further, we utilized a *B. subtilis* 1981 reporter strain in which the GFP-MinD is recruited to the poles and the septum in cells with intact membrane potential. We observed MinD delocalization already within 2 min of treatment (Figure S3A), further validating membrane depolarization as primary cellular effect of DHG.[21]

To understand the cause of observed membrane depolarization, we first measured extracellular [K^+] in a time-dependent manner using a K^+-selective electrode (Figure 3B), followed by quantification of intracellular K^+/Na^+ concentrations via elemental analysis (inductively coupled plasma mass spectrometry, ICP-MS) (Figure 3C). We observed an immediate increase of extracellular [K^+] (Figure 3B) after addition of DHG, reaching maximal concentration after approximately 2 min (10 μg/mL/24 μM) or 8 min (1 μg/mL/2.4 μM) in a concentration-dependent manner. Notably, concentrations used in this assay are higher than regular MIC as it was performed using high cell density (OD_{600} = 3, corresponding to $\geq 10^9$ CFU/mL) to achieve [K^+] above electrode detection limit. As positive control, we used membrane toxin melittin, which induced an even faster response, as maximal K^+ efflux was reached within less than 10s. Concordantly using ICP-MS, we confirmed a drastic impact of DHG on intracellular ion concentration, with [Na^+] increasing 10-fold while [K^+] drops almost below detection limit after 30 min treatment (Figure 3C).

To assess the influence of salt ions on bacterial susceptibility toward DHG treatment, we determined MICs in medium containing elevated levels of [Na^+] and/or [K^+] (Figure 3D). We found that 400 mM K^+ almost completely abolishes DHG activity, as the MIC increased 64-fold against *S. aureus* and even >256-fold for *E. faecium*. This effect almost entirely disappeared in *S. aureus* at 50 mM K^+ (2-fold), while it was still pronounced in *E. faecium* (128-fold). With high [Na^+] however, DHG activity was enhanced 2-fold in *S. aureus* and even 4-fold in *E. faecium*. Both ions at 200 mM diminished activity of DHG, ultimately suggesting K^+-efflux as the major factor driving chlorotonil activity in bacteria. For malaria parasites, disruption of the salt ion concentration has been described as MoA of cipargamin, which disrupts sodium homeostasis in *P. falciparum* by acting on PfATP4, a P-type Na-ATPase.[22,23] Therefore, the influence of [Na^+] and [K^+] on the activity of ChA, and the sensitivity of a cipargamin-resistant strain were assessed (Table S2). In *P. falciparum*, only a minor effect on the activity could be observed using the highest concentration of NaCl and KCl tolerated by the parasites *in vitro* (20 mM), while a clear effect could be seen for cipargamin. Neither were any effects observed for DHG-susceptibility of the cipargamin-resistant *P. falciparum* carrying mutations in the known drug target PfATP4 (sodium ATPase) (Table S2).

We further checked if we can restore bacterial growth upon addition of 400 mM potassium to *S. aureus* treated with DHG for 1.5h or 8h. After 1.5h treatment, growth quickly resumed after addition of K^+, while it took more than 10h to resume after 8h exposure to 8-fold MIC (Figure 3E). We could re-establish growth up to 16-fold or 8-fold MIC, when treated for 1.5h or 8h prior K^+-addition, respectively (Figure S3B). The time-kill kinetic in presence of 400 mM K^+ (Figure 3F) showed initially a rapid CFU reduction (>$5\log_{10}$) within 1h treatment at 8xMIC, followed by a fast growth recovery to >10^8 CFU/mL after 5h treatment. Importantly, after the initial reduction, the increase in CFU on agar

(H) Live-dead staining using Syto9 (green) and propidium iodide (PI, red) of *S. aureus* treated with DHG for 1h, shows intact cytoplasmic membrane (CM) (n > 100 cells, mean with SD shown).
(I) FM5-95 staining (lipid membrane visualization) using *Bacillus subtilis* 168 treated with DHG; cell swelling is indicated by arrows. Scale bar 10 μm. *p < 0.05, ***p < 0.001, ****p < 0.0001.

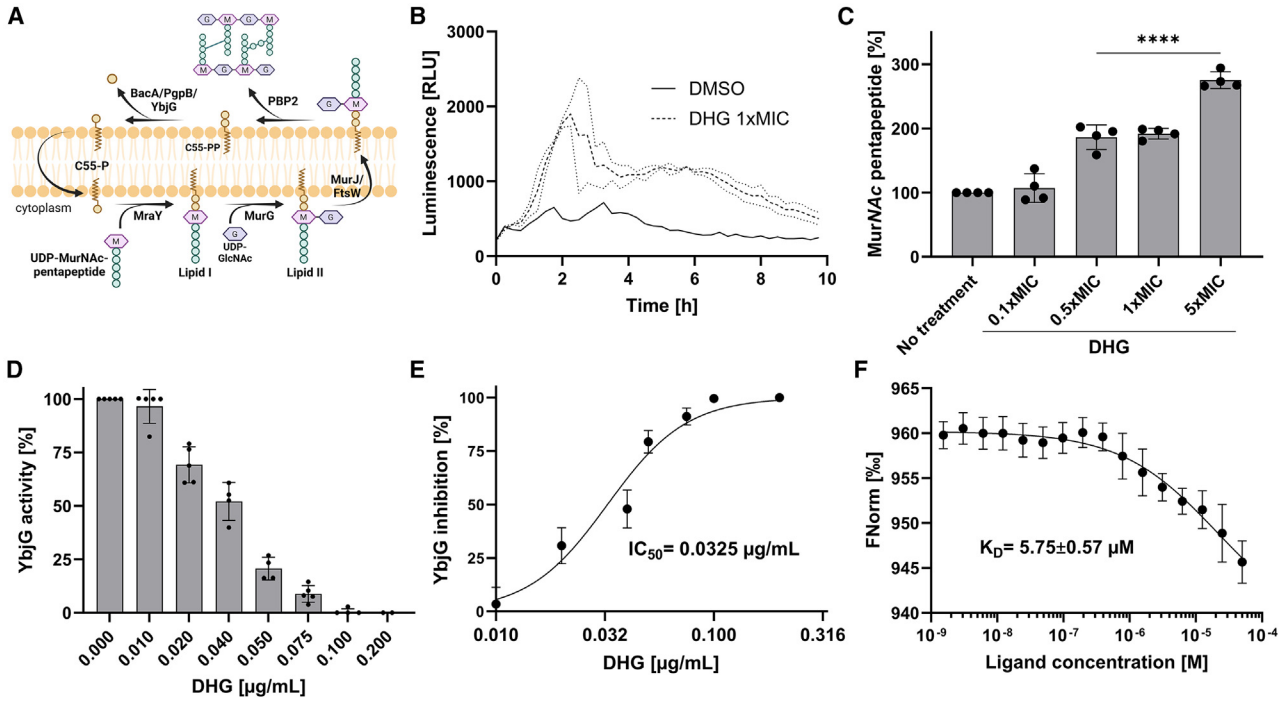

Figure 2. DHG affects cell wall synthesis by direct binding of YbjG

(A) Peptidoglycan synthesis overview, created with Biorender.

(B) *B. subtilis* lia-lux cell wall stress reporter strain shows weak response after DHG treatment, mean and SD are shown ($n = 2$). Vancomycin results in 17,600 RLU.

(C) Intracellular accumulation of UDP-MurNAc pentapeptide in *S. aureus* HG001 following DHG-treatment. DMSO was set to 100%, with mean and SD shown ($n = 4$), compared using one-way ANOVA. Vancomycin results in 1800%.

(D) DHG inhibits the YbjG-catalyzed reaction from $C_{55}PP$ to $C_{55}P$. The reaction without DHG was set to 100% ($n = 4$, with mean and SD shown).

(E) Corresponding functional inhibition from D, with mean and SD shown.

(F) MST measurements of YbjG treated with DHG, mean and SD are shown ($n = 3$). ****$p < 0.0001$.

($>5\log_{10}$ units) did not correlated with the increase in respective optical density (A_{600}: 0.25 to 2), indicating that the CFU increase observed did not solely result from new bacterial growth, rather than that bacteria did recover from a DHG-induced viable-but-non-culturable state (VBNC). Concordantly, we also observed small-colony-variants of regrown *S. aureus* after treatment in K^+-supplemented medium (Figure S3C).

Proteomic profiling reveals an effect on potassium homeostasis and the secondary target MetAP

We hypothesized that uncontrolled K^+/Na^+ flow across the membrane is the underlying principle behind the MoA of chlorotonils in bacteria and performed proteomic analysis of *S. aureus* to gain a better insight into the protein changes induced by chlorotonil treatment. We performed both full proteome analysis and thermal proteome profiling (TPP) of chlorotonil-treated *S. aureus* (Figure 4).

For full proteome analysis (Figure 4A), we exposed cells to sub-MIC concentration of DHG (0.2-fold MIC) and compared them with DMSO-treated cells. Significantly dysregulated proteins were further analyzed using String Network (Figure S4A). We found 16 and 26 proteins with significantly increased or decreased abundance, respectively. For the ease of description, we refer to them as up-/downregulated proteins. Among upregulated proteins, all proteins of the main potassium uptake system KdpABC ($\log_2$ fold-change of 1.8–1.9, cluster strength: 2.13), as well as some secreted bacterial hemolysins (cluster strength: 1.19), showed significant functional enrichment in the String Network (Figures 4A and S4A). Further, SA2153 (uncharacterized transcriptional regulator, $\log_2$ fold change of 3.0) and SA0221 (complement inhibitor SCIN, $\log_2$ fold change of 2.41) were found upregulated. Three of the most strongly downregulated proteins in *S. aureus* were BetA, GbsA, and CudT, all involved in the biosynthesis of the prokaryotic osmoprotectant glycine betaine (GB); however, no significant functional enrichment could be detected within the network using the String database tool. Overall, we confirmed a cellular response to dysregulated monovalent cation homeostasis on protein level in cells exposed to DHG.

We set out to investigate further potential protein targets and general effects using TPP (Figures 4B and S4B).[24–26] _S_SIn total, eight proteins were stabilized and passed all criteria, while eight proteins were significantly destabilized.

Among significantly destabilized proteins are three ribosomal proteins (*rplB*, *rplC*, and *rplF*) and the D-Ala-D-Ala ligase, while the most stabilized protein SAUSA300_0362 was KefA, a small conductance mechanosensitive ion channel protein (Figure S4B). Further, glycosyl transferase BsaH (SAUSA300_1349), that utilizes UDP-GlcNAc as substrate as part of cellular redox balance,[27] also showed significant stabilization upon treatment. All TPP hits with available transposon mutants (Nebraska USA300 library, non-essential proteins) were tested against

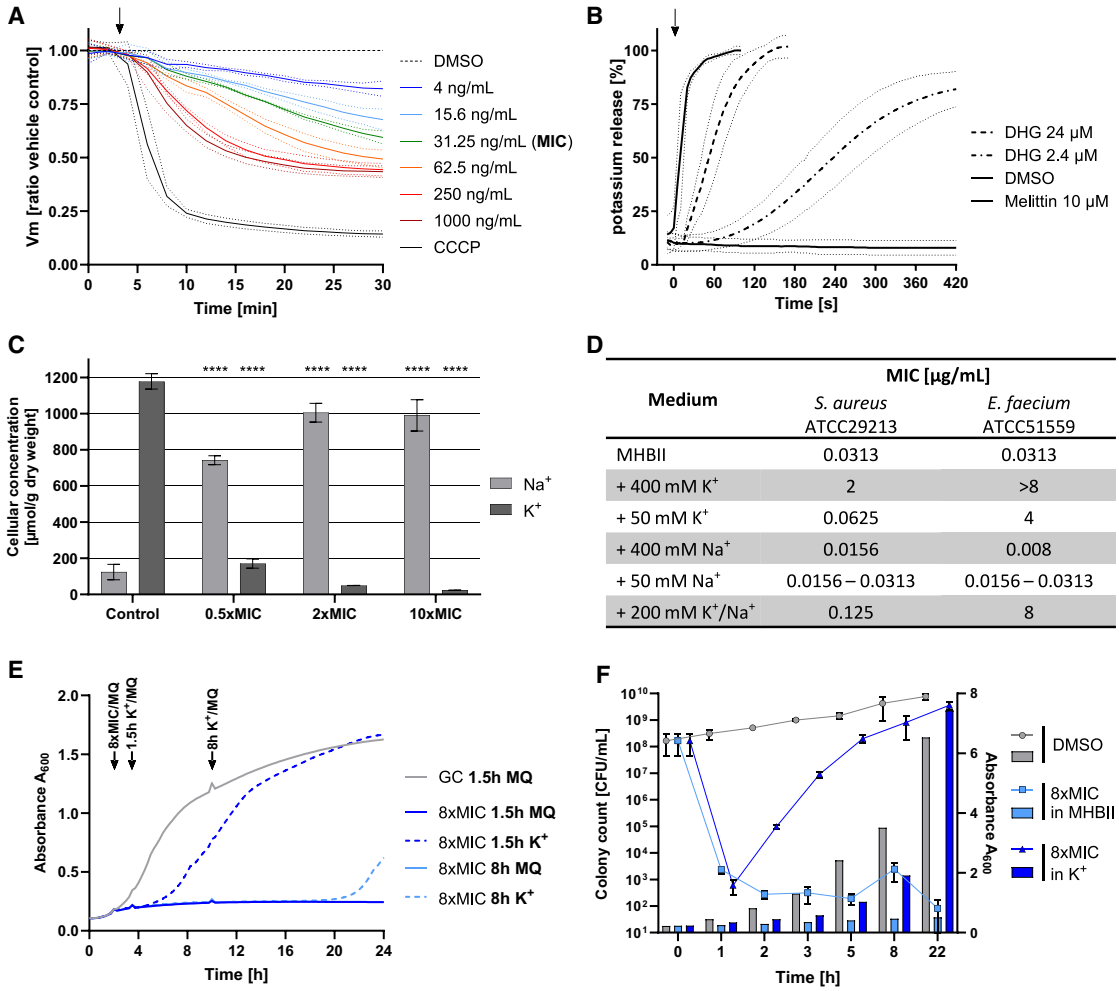

Medium	MIC [µg/mL]	
	S. aureus ATCC29213	*E. faecium* ATCC51559
MHBII	0.0313	0.0313
+ 400 mM K^+	2	>8
+ 50 mM K^+	0.0625	4
+ 400 mM Na^+	0.0156	0.008
+ 50 mM Na^+	0.0156 – 0.0313	0.0156 – 0.0313
+ 200 mM K^+/Na^+	0.125	8

Figure 3. Chlorotonils cause immediate membrane depolarization and affect ion homeostasis

(A) $DiOC_2(3)$ assay using DHG and *S. aureus*. Compound was added at indicated time point (arrow) and red/green fluorescence ratio was normalized against DMSO treated control cells, mean and SD shown ($n = 3$).

(B) Potassium efflux of *S. aureus* ($OD_{600} = 3$) treated with DHG or melittin, measured using a K^+-selective electrode with mean and SD shown ($n = 3$). Arrow indicates compound addition; 24 µM DHG equals 10 µg/mL.

(C) Elemental analysis of intracellular [Na^+] and [K^+] after 30 min treatment using DHG normalized against pellet dry-weight, mean and SD are shown ($n = 3$), compared using one-way ANOVA.

(D) Susceptibility assay using DHG in presence of different salt concentrations ($n = 2$).

(E) Growth rescue experiment reveals that *S. aureus* growth can be restored upon addition of 400 mM K^+. Cells were grown for 2h prior addition of 8-fold MIC (compare Figure S3B) DHG (or DMSO) (first arrow). Potassium (or de-ionized water, MQ) was added after 1.5h (second arrow) or 8h (third arrow) of DHG treatment.

(F) Time-kill curve of *S. aureus* ($OD_{start} = 0.25$) treated with 8-fold MIC DHG (or DMSO) either in regular MHBII or in MHBII supplemented with 400 mM K^+; lines show colony count, bars represent respective optical density (A_{600}). See also Figure S3. ****$p < 0.0001$.

DHG, but no MIC shift could be observed for any of them, which prompted us to deprioritize them as target proteins contributing to primary activity.

The methionine aminopeptidase (*map*, MetAP) is the only stabilized protein that is essential for growth (Figure 4C). To investigate the potential impact of chlorotonils on MetAP activity, the *map* gene from *S. aureus* USA300 (SAUSA300_1869) was recombinantly expressed, purified, and used for *in vitro* activity assays with cobalt as cofactor (Figure 4D).[28–30] The release of cleaved *para*-nitroanilide from methionine-*p*-nitroanilide (MetpNA) was measured, the linear range fitted, and the slopes calculated (D). Chlorotonils inhibited the *Sa*MetAP in a dose-dependent manner, while fumagillin, a human MetAP-2 inhibitor also showed inhibition of *Sa*MetAP with similar molar ratio. As MetAP inhibitors often bind metal ions, we checked for chelator activity of chlorotonils and successfully grew crystals containing two or three DHG molecules coordinating one copper, cobalt, or aluminum ion through their di-keto moiety, indeed confirming chelator effects of DHG (Figure S5). To test whether the observed MetAP inhibition is merely due to a cofactor depletion, rather than direct inhibition of the protein, the assay was repeated with a 16-fold molar excess of $CoCl_2$ (normal set-up

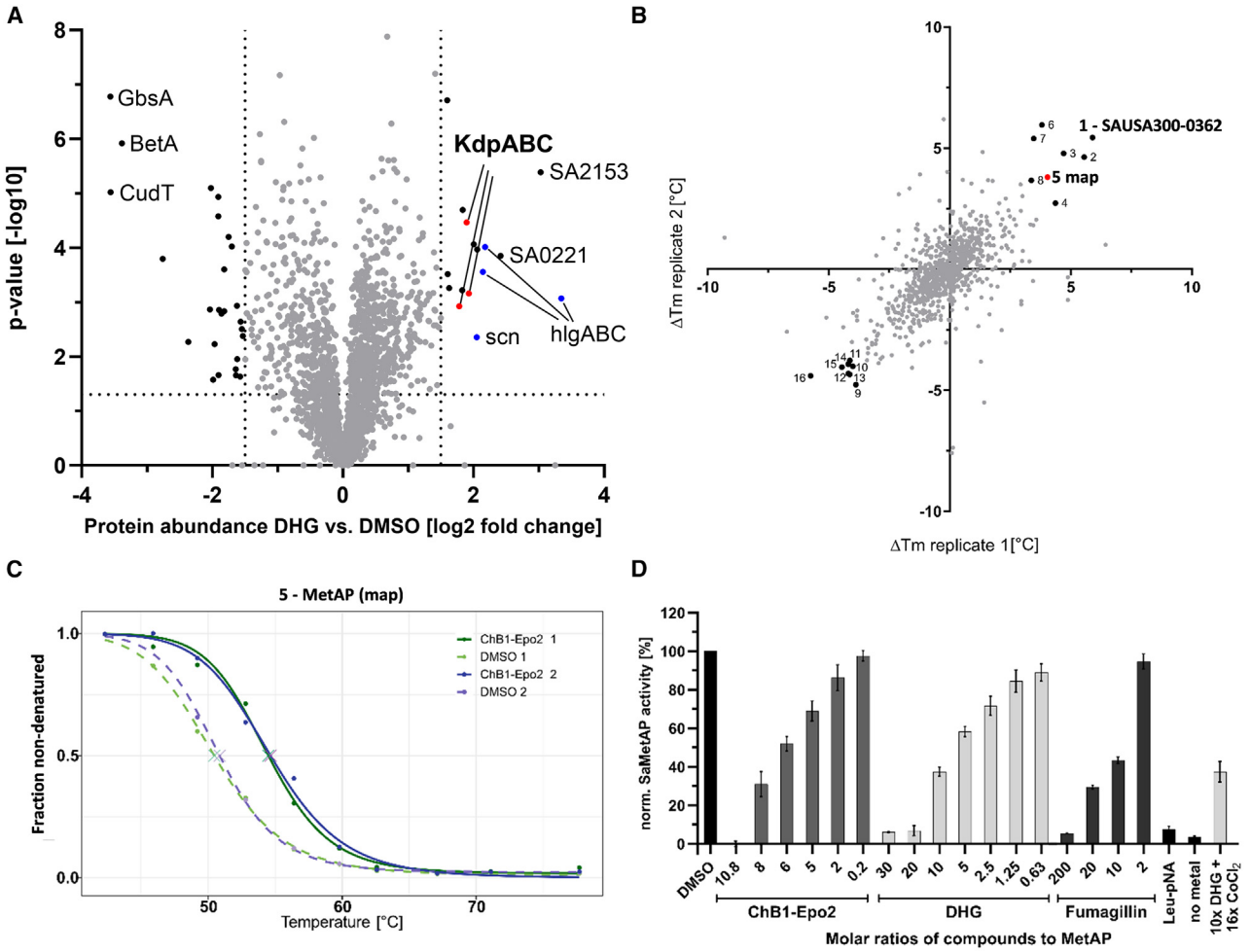

Figure 4. Proteomic profiling reveals an effect on potassium homeostasis and the secondary target MetAP

(A) Full proteome analysis of *S. aureus* with expression changes of DHG-treated cells (0.2-fold MIC) compared to untreated cells. Significant up-/downregulation was analyzed by a two-tailed Student's t test with *p*-value [$-\log_{10}$] > 1.3 (horizontal line) and abundance difference [$\log_2$] > 1.5 as cut-off (n = 4).

(B) Thermal shifts (ΔT_m) between treated (ChB1-Epo2) and untreated *S. aureus* cells in both replicates are displayed. All proteins that passed all significance criteria were numbered – refer to Figure S4B.

(C) Melting curves of MetAP (red dot in B, 5), the only stabilized protein essential for growth (n = 2).

(D) SaMetAP activity assay, with slopes normalized to their respective DMSO control. The enzyme is inactive without addition of $CoCl_2$ and it specifically cleaves only Met-pNA and not the leucine derivative Leu-pNA. The assay was performed in at least 2 independent replicates, consisting of 3 technical triplicates, mean and SD are shown. See also Figures S4 and S5 and Table S3.

3-fold), and we observed the same inhibition as before (Figure 4D). Notably, *Sa*MetAP is slightly inhibited by higher $CoCl_2$ concentrations, so a respective control was included and used for normalization. Despite serious efforts, co-crystallization attempts failed due to limited solubility of chlorotonils. MetAP inhibition alone should not explain the primary activity of chlorotonils, and to confirm, we studied the role of MetAP in *S. aureus* RN4420 using an antisense library, where expression levels of individual genes can be regulated by different xylose concentrations. As expected, controlled MetAP expression did not induce any change in DHG susceptibility (Table S3).

Ultimately, the depolarization described above provides the primary reason for phenotypic bacterial killing by DHG, but direct interaction partners of chlorotonils remained elusive. To gain additional insights into molecular targets of the chlorotonils, we next performed a resistance-guided approach, i.e., genome-sequencing of *in vitro* generated DHG-resistant *S. aureus* mutants.

Resistance to chlorotonil is mediated by FarR/FarE overexpression

To gain insights into molecular targets of chlorotonils, we aimed to evolve resistance in *S. aureus* ATCC29213. Therefore, we tried to determine the frequency of resistance (FoR) using a standard setup with selective agar supplemented with 4- and 8-fold MIC of DHG, but we failed to isolate any resistant clones and thus could not determine FoR under standardized conditions. We then used long-term exposure and adaptation (LEA),[31] to adapt bacterial cells slowly to chlorotonil using sub-MIC concentrations. After several passaging rounds, we were able to generate chlorotonil-resistant (Ch^R) *S. aureus* and observed more than

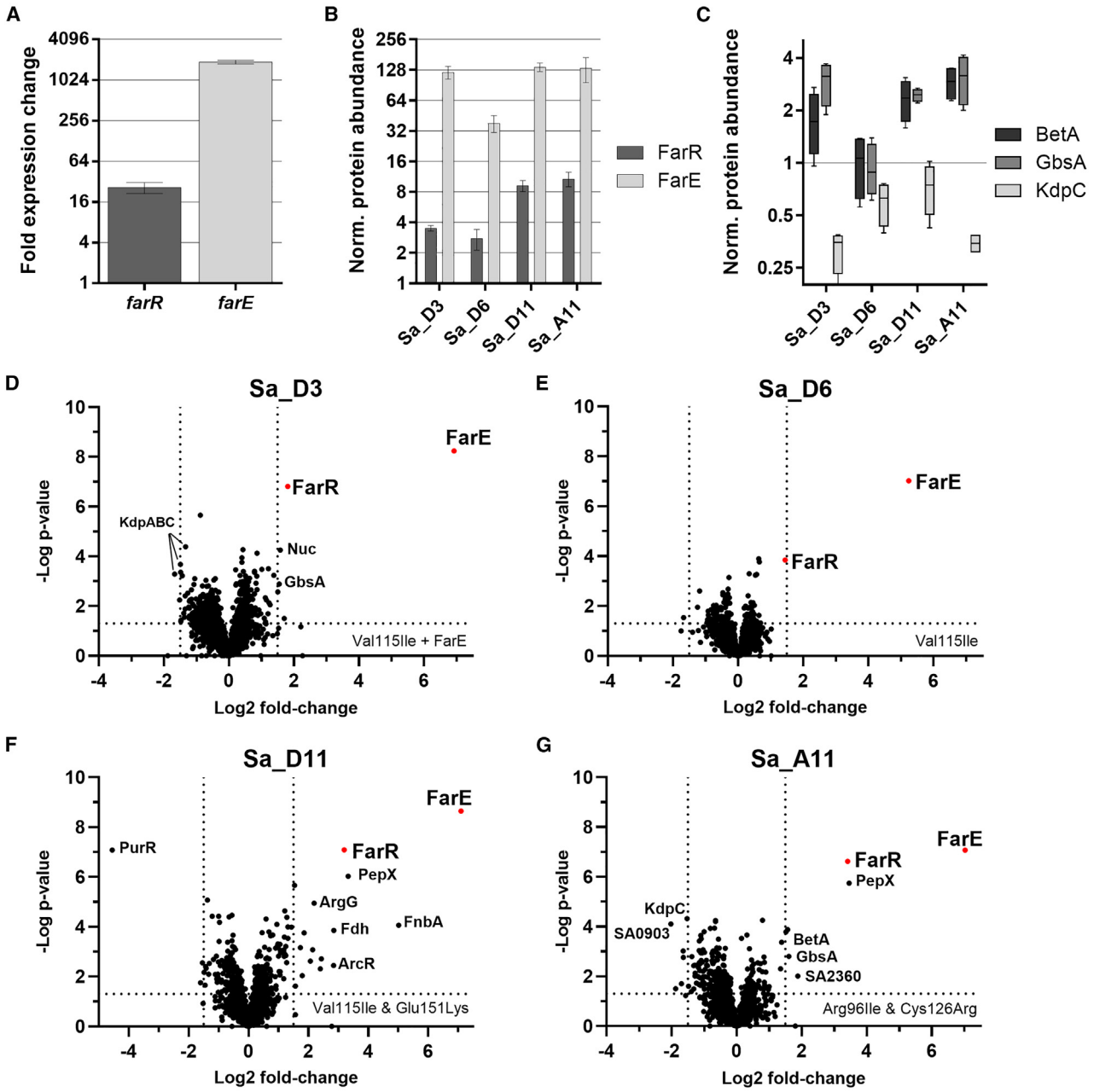

Figure 5. Ch^R *S. aureus* shows overexpression of the major lipid efflux pump FarE

(A) Gene expression of *farR* and *farE* in Sa_D11 (n = 2, mean and SD shown).

(B) Upregulation of FarR and FarE in full proteome analyses of Ch^R *S. aureus* mutants; mean and SD are shown (n = 4).

(C) Dysregulation of BetA, GbsA, and KdpC in Ch^R *S. aureus* expressed as fold change normalised against wildtype; mean and SD shown (n = 4).

(D–G) Full proteome analyses of mutant strains compared to wildtype *S. aureus*. Significant up-/downregulation was analyzed by two-tailed Student's t test with p-value [-log$_{10}$]>1.3 (horizontal line) and abundance difference [log$_2$]>1.5 as cut-off (n = 4). Respective genomic mutation in *farR* are displayed within the diagram. See also Tables S4 and S5.

64-fold MIC shift within one week of LEA. As reference, we used clinically approved ofloxacin (OFX), which in the same time also resulted in a 64-fold shift in susceptibility (not shown). Mutants generated in presence of DHG were cross-resistant to ChA (up to >64-fold) and vice versa, however, mutants Sa_D6 and D8 showed only an 8- to 16-fold shift in susceptibility to ChA (Table S4). Resistance phenotypes were stable after ten rounds of non-selective passaging. Isolated LEA mutants were sequenced and analyzed for single nucleotide polymorphisms (SNPs) or other genotypes (Tables S4 and S5).

All mutants (n = 24) carried mutations in *farR*, encoding the negative regulator of the FarE fatty acid and lipid efflux pump

(Table S4). Six mutants carried two different mutations within *farR*, while the remaining isolates carried one SNP only. Mutations resulting in an exchange of valine to isoleucine at position 115 (Val115Ile) were found in 12 of 24 isolates, while Glu151Lys was found in eleven. Additionally, eight mutants also carried SNPs in the intergenic region between *farR* and *farE*. Further, we identified mutations in ribosome associated GTPase HflX (n = 8), alanine dehydrogenase Ala (n = 8), malate:-quinone oxidoreductase Mqo2 (n = 7), *trans*-aconitate 2 methyltransferase Tam (n = 5), and in *pur*-operon repressor PurR (n = 4) (Table SI5) with no direct correlation to resistance phenotypes.

In the literature, *farR* mutations are reported to convey resistance to rhodomyrtone (ROM), a membrane-active antibiotic inducing cell lysis.[32,33] We observed that Ch^R *S. aureus* were also resistant to ROM (>64-fold, Table S4), suggesting a similar lipid-mediated resistance mechanism via FarE overexpression. To confirm, Ch^R Sa_D11 (FarR: Val115Ile & Glu151Lys), was selected for qPCR analysis. In this mutant, we found *farR* upregulated 25-fold, while *farE* expression increased approximately 2000-fold when compared to the wildtype (Figure 5A). We then selected four mutant strains (Sa_D3, Sa_D6, Sa_D11, and Sa_A11) covering different genotypes for full proteome analyses (Figures 5B–5G). Sa_D3, D6 and D11 carry Val115Ile in FarR, while D11 also carries Glu151Lys, and D3 also carries mutations in the intergenic region to *farE*. With Sa_A11, we covered Arg96Ile and Cys116Arg mutations within FarR. On average, we found FarR 7-fold and FarE over 100-fold upregulated when compared to wildtype (Figure 5B), confirming the expression changes also on proteome level. In Sa_D6, FarE was only 40-fold upregulated, potentially explaining the medium-level resistance conferred by only a single mutation in FarR (32-fold change in MIC compared to WT). In contrast, the other investigated mutant strains were far-less susceptible (>64-fold shift in MIC) and carried either two mutations in *farR* (Sa_D11 and Sa_A11) or an additional mutation close to *farE* (Sa_D3). These high-level-resistant mutants also showed BetA/GbsA abundance approximately 2- to 3-fold increased, and KdpC 2-fold decreased, respectively (Figure 5C). Sa_D11, which carries additional *purR* mutations, showed 20-fold reduced abundance of PurR, while FnbA and B (negatively controlled by PurR) were upregulated 30- and 3.5-fold, respectively.

DHG binds to membrane lipids and fatty acids but cross-reactivity does not induce adverse effects in mice

Mutations in a fatty acid and lipid efflux system prompted the question whether chlorotonils bind directly to membrane lipids. We added prominent representatives of FAs (lauric, myristic, pentadecanoic, palmitic, palmitoleic, stearic and linoleic acid, respectively) and lipids (1-**p**almitoyl-2-**o**leoyl-*sn*-glycero-3-**p**hosphatidyl**g**lycerol/-**c**holine/-**e**thanolamine/-**s**erine: POPG, POPC, POPE, POPS; lysyl phosphatidyl**g**lycerol, LPG) to *S. aureus* susceptibility assays confirming an influence on DHG activity (Table S6). We could observe up to 16-fold reduced activity of DHG in the presence of 100 μM saturated FAs/lipids, while the effect of adding unsaturated FAs was overall less pronounced. Generally, only minor effects on DHG activity could be attributed to the presence of different lipid head groups.

To study the biophysical interaction of DHG with FAs and lipids, respectively, and to determine K_D, we tested both isothermal titration calorimetry (ITC) and surface plasmon resonance (SPR); unfortunately, both methods were not suitable due to solubility limits or unspecific binding to the reference cell surface. As proof of concept, we then applied native-lipid mass spectrometry, which confirmed a direct interaction of DHG with all tested membrane lipids. We could detect masses corresponding to DHG plus lipid mostly as sodium or potassium adducts and confirmed DHG mass losses in MS/MS fragment spectra (Table S7). Exemplary, POPE is shown in Figures 6A–6C. We further detected the presence of DHG multimers (Figure 6A, third panel). To understand potential consequences of such lipid interactions, we measured the specific membrane capacitance of an artificial POPG membrane generated in a microfluidics device (Figures 6D and S6A). We detected a significant increase in specific membrane capacitance in presence of DHG and thus, for the first time, confirmed protein-independent membrane effects.

Our results suggested a direct lipid interaction as primary reason for chlorotonil activity and obviously raised the question of cross-species reactivity with eukaryotic cells. Upon screening of different cell lines, we found IC_{50} values ranging from 5.4–9.8 μM for HEK293, HCT116 and CHO-K1, exceeding c_{max} of around 2.4–4.8 μM *in vivo* (Figure 6B and 6C and Hofer et al., 2024),[12] resulting in selectivity indices (SI) from 70 to 128 when compared to *S. aureus*. Again, HepG2 was non-susceptible (>90 μM, SI > 1184), as previously published.[12] For proof of concept, we checked if cytotoxicity is caused by potassium leakage akin to bacterial cells, and treated eukaryotic cells with non-physiological concentrations of DHG (24 μM); after 30 min, we again measured extracellular [K^+] (Figure S6B). For normalization, melittin at lytic concentrations was used and set to 100%. Higher K^+-release was observed in HEK293 (95.4% compared to melittin) and HCT116 (84.1%), while CHO-K1 (43.1%) and HepG2 (22.2%) were less affected; in general, no lytic behavior could be observed for DHG. We followed up by testing K^+-release from erythrocytes treated with 0.1–10 μg/mL DHG (0.24–24 μM, Figure 6E), and found only a mild increase (18%, p = 0.006) in extracellular [K^+] from erythrocytes treated with 10 μg/mL, while lower concentrations were non-significant.

In previous studies, we demonstrated good tolerability (and antibacterial efficacy) of DHG in zebrafish larvae and various mouse models,[10–13] however, in view of our recent findings in eukaryotic cells, we set out to further de-risk the application of DHG in mice. For this, mice were treated with doses of DHG that had been shown to be efficacious (e.g., in significantly increasing survival in a bloodstream infection model)[12] on four consecutive days using either intravenous (i.v.) or subcutaneous (s.c.) application, with daily blood sampling to determine DHG levels (Figure S6C) and terminal blood sampling for clinical chemistry. During the 5-day study, none of the animals showed an abnormal behavior, and total doses of 20 mg/kg (i.v.) and 100 mg/kg (s.c.; with c_{max} of 1.75 μg/mL), respectively, were well tolerated with no significant accumulation effect. Determining blood [K^+], we did not detect significant effects in the treatment group compared to vehicle and mock-treated control groups despite DHG blood concentrations above *S. aureus* MIC (Figures 6E and S6C).

DISCUSSION

Chlorotonils, first described in 2008, are broad-spectrum antimicrobials acting against Gram-positive bacteria and *Plasmodium*

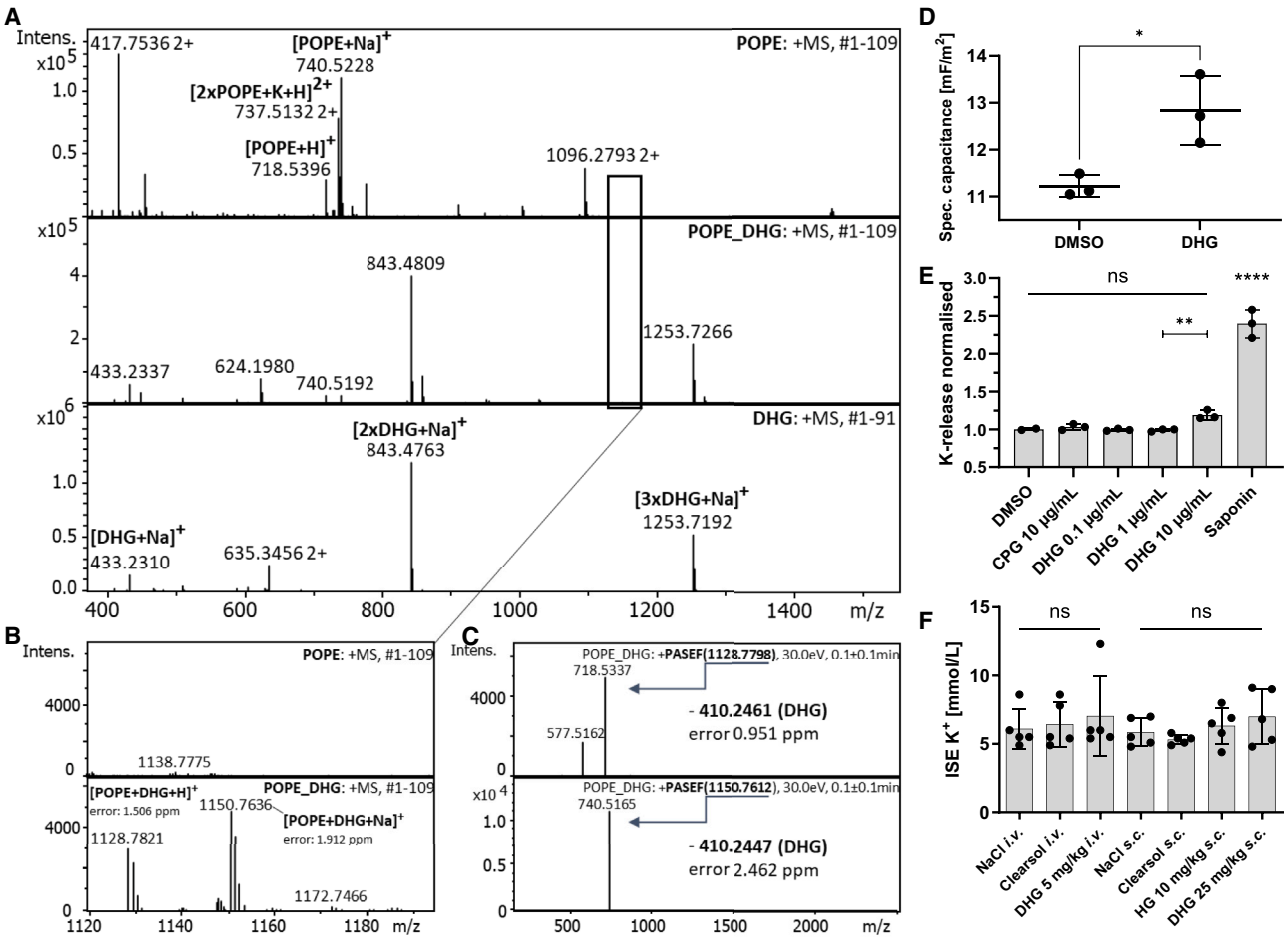

Figure 6. DHG binds membrane lipids but cross-reactivity does not induce pathological effects *in vivo*

(A) Mass spectra of POPE (top), POPE/DHG in 1:10 ratio (middle) and DHG (bottom) after direct infusion using native lipid mass spectrometry.

(B) Close up of panel A (POPE and POPE/DHG) for 1120 to 1190 m/z shows presence of new masses 1128.7821 m/z $[POPE+DHG]^+$ and 1150.7636 m/z $[POPE+DHG+Na]^+$ in POPE/DHG.

(C) MS/MS fragment spectra (PASEF) of 1128.7798 m/z (top) and 1150.7612 m/z (bottom) confirm masses of POPE monomers (as $[M + H]^+$ or $[M+Na]^+$) and loss of DHG monomers (exact mass: 410.24571 Da).

(D) Increase in specific membrane capacitance of artificial POPG membrane in presence of DHG, utilizing microfluidics. Mean and SD are shown (n = 3), compared using Student's t test.

(E) Potassium release from erythrocytes treated for 30 min with DMSO, cipargamin (CPG), DHG, and saponin (positive control) normalized against DMSO. Mean and SD are shown (n = 3), compared using one-way ANOVA and Student's t test.

(F) Non-significant change in potassium serum concentration in mice treated for four consecutive days using saline, Clearsol vehicle, or DHG in indicated concentrations either intravenously (i.v) or subcutaneously (s.c). Terminal blood sampling was performed at day 5, mean and SD are shown (n = 5) and compared using one-way ANOVA. See also Figure S6 and Table S7. *: $p < 0.05$, **: $p < 0.01$, ****: $p < 0.0001$.

falciparum.[10,34] Until now, their unique mode of action remained elusive. We report here the first concise study of this natural product class's MoA, using a semisynthetic lead structure with enhanced properties called dehalogenil (DHG).[12] We provided a series of microbiological, biochemical, and analytical data to confirm chlorotonils as membrane-active antibiotics. We postulate a complex MoA in *S. aureus* and found at least two additional enzyme targets inhibited by chlorotonils (Figure 7). They induce dysregulated monovalent cation transport leading to membrane depolarization, and potentially target both peptidoglycan and protein biosynthesis via YbjG and the methionine aminopeptidase (MetAP). We postulate lipid-mediated protein-independent membrane activity as the main driver of chlorotonil activity against Gram-positive bacteria.

Initial microbiological profiling revealed a fast onset of action, reducing bacterial growth within minutes after treatment. We found significant inhibitory activity below the regular MIC in the single-digit nanomolar range and even against efflux-deficient *E. coli* with impaired outer membrane, and for the first time confirmed activity also against *M. tuberculosis*. These characteristics excluded most MoA hypotheses, as only few targets can explain immediate, yet non-lytic activity. A membrane-targeting activity appeared likely, as such mechanisms have been seen for antimicrobial peptides and small molecules, characterized by

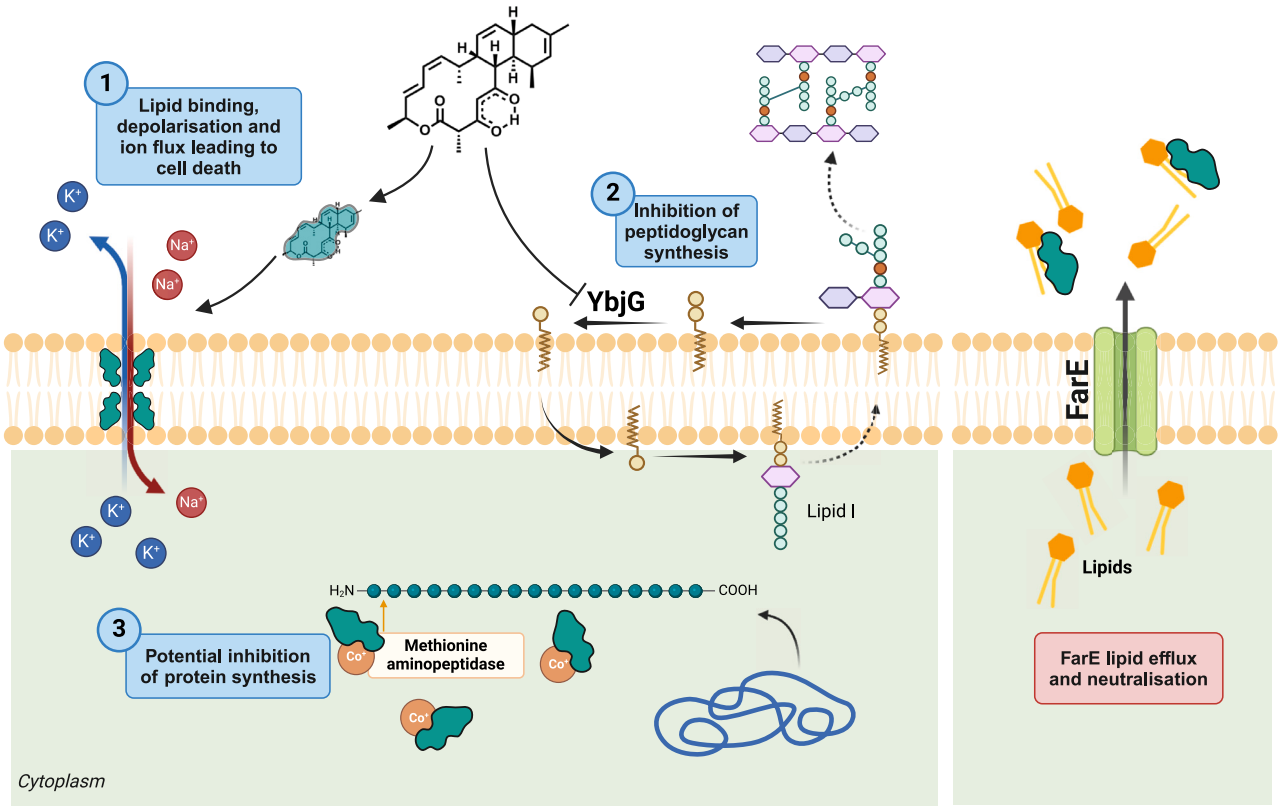

Figure 7. Complex mode of action (blue) of chlorotonils involves membrane depolarization, as well as secondary effects targeting peptidoglycan and protein biosynthesis

Resistance (red) is mediated by lipid-efflux-detoxification of DHG at the outside of the cell via FarR/FarE. Created in BioRender. Deschner, F. (2025) https://BioRender.com/yd98h0q.

similar killing profiles.[35] Our studies confirmed immediate membrane depolarization mediated by increased potassium efflux, without physically destroying the membrane barrier through *e.g.*, large pore formation or lysis. Concordantly, the antibacterial activity of chlorotonils was sensitive to high [Na^+] and/or [K^+], while proteome analysis confirmed the upregulation of K^+-uptake upon treatment. These results align with a transcriptomic study performed in *C. difficile*, where potassium transport ATPase subunits (KdpAB) were also upregulated following treatment with ChB1-Epo2.[13]

Disruption of membrane potential has detrimental effects on cell physiology[35–37] and can be the sole reason for primary antibacterial activity of zhlorotonils, likely extending to anthracimycin due to their structural similarities.[15,16] However, depolarization is not necessarily immediately bactericidal (suggested by > 3-$\log_{10}$ CFU reduction in time-kill experiments), and might render cells in a viable, but non-culturable state (VBNC) prior eradication. This aligns with the regrowth at sub-MIC, the possibility to re-establish growth upon K^+-addition, and the presence of small-colony-variants in presence of K^+. Thus, the classical definition – 3-$\log_{10}$ reduction in CFU equals bactericidal activity – might be difficult to apply to chlorotonils. This is supported by previous *Clostridium* studies, where we reported inhibition of endospore outgrowth after chlorotonil-treatment that could be re-established using isopropanol washing of treated endospores.[13]

The major remaining questions were if the depolarizing activity is completely protein-independent, and if other enzyme targets are addressed. While characterizing membrane activity, we observed cell wall weakening and identified YbjG as one target of DHG, a protein required for peptidoglycan biosynthesis.[19,20] To our knowledge, DHG is the first described direct inhibitor of YbjG in literature. While YbjG inhibition might explain the de-/stabilization of the D-Ala-D-Ala ligase and BshA in TPP, it cannot explain the fast depolarizing effects as it only plays a role during bactoprenol recycling and can be compensated for by undecaprenyl pyrophosphate phosphatase UppP.[19,20] Hence, the involvement of YbjG inhibition in chlorotonil MoA requires further investigation suggesting only a secondary role. Additionally, TPP revealed further potential protein partners of chlorotonils, including a non-essential potassium pump KefA and the protein biosynthesis protein MetAP.[38] Generally, TPP can be used for studying direct target engagement, while it also delivers information about secondary effects, and can give insights into protein-protein interactions and conformational shifts.[25,39–41] Although KefA, a putative MscS family potassium channel, fits to the disruption of potassium homeostasis, validated transposon-knockouts did not show a change in susceptibility, deprioritizing the K^+-efflux pump as a direct antibacterial target. KefA participates in osmotic pressure regulation and is sensitive to voltage, membrane tension, and membrane potential.[42,43] We conclude

that depolarization likely influences the channel downstream and thus can lead to changes in its thermal stability. The role of significantly de-/stabilized non-essential proteins was not investigated further, but we could clearly demonstrate that chlorotonils inhibit MetAP. While the MetAP is an interesting therapeutic target and expanding the chemical space of such inhibitors could lead to new classes of antimicrobials, the rapid onset of action of chlorotonils cannot be caused by MetAP inhibition.

Following challenging *in vitro* resistance development in *S. aureus*, we identified mutations in the FarR/FarE fatty acid and lipid efflux system, similar to membrane-active rhodomyrtone (ROM).[32,33,44] Ch^R mutants overexpress FarE showing cross-resistance to ROM, suggesting a similar lipid-mediated mode of resistance (MoR), suggesting a lipid-mediated MoA for chlorotonils. Supplementation of the test medium with typical representatives of lipids and FAs, reduced DHG activity *in vitro*, with saturated FAs being more effective in decreasing activity rather than those with unsaturated acyl chains, while lipid head groups had only a minor influence. With FarR being highly conserved across the *S. aureus* pan-genome (AureoWiki),[45] FarE-mediated resistance could therefore play a role in clinical isolates. However, lipid efflux-mediated neutralization is rare and so far not observed in clinical settings,[46] but nevertheless, it was described for daptomycin resistance in *agr* knockout strains.[47] Basal FarE activity seems insufficient to confer resistance as we have not identified any non-susceptible clinical isolate (including daptomycin-resistant strains) of *S. aureus* so far.[12] Here, even 40-fold upregulation of FarE only resulted in medium-level resistance in Ch^R mutants, questioning the *in vivo* relevance of FarE-mediated detoxification. Given the anti-mycobacterial activity, it is important to consider that FarE is part of the MmpL protein family, consequently, MmpL-mediated resistance mechanisms in *M. tuberculosis* should be taken into account and will be evaluated in future studies.[48] Currently we cannot explain why Ch^R *S. aureus* is high-level resistant (>64-fold MIC shift), while FA supplementation resulted in 16-fold reduced activity. Possibly, we have not yet identified the prime binding partner, but trial-and-error-testing of lipids, FAs, or other membrane components was considered unfeasible for now and will require further exploration. We also cannot exclude a role of other factors which we found dysregulated in DHG-resistant mutants, like proteins involved in purine/glycine betaine biosynthesis, which were also described in previous studies in chlorotonil-treated *C. difficile*.[13,49–52] Generally, we conclude that the fast-acting kinetic makes resistance development against chlorotonils difficult and only possible when exposed to sub-inhibitory concentrations.

Physicochemical limitations of chlorotonils rendered both ITC (solubility issue) and SPR (binding to reference cell surface) unsuitable to study chlorotonil-lipid interactions. We then relied on native lipid mass spectrometry to confirm direct non-covalent binding. We indeed observed signals representing combined masses of lipids and DHG with corresponding MS/MS fragment spectra, and also confirmed changes in specific membrane capacitance utilizing an artificial POPG membrane. Further biophysical interaction studies should be performed to better understand the membrane activity of chlorotonils, as three models of membrane activity have been proposed for AMPs.[35] Although developed for AMPs, we may be able to use them to describe our understanding of chlorotonil activity. The carpet model (requiring high compound concentration and lytic activity) seems incompatible with chlorotonils nanomolar, non-lytic behavior. Both the barrel stave model and the toroidal model assume pore formation, although the latter requires initial lipid head group interaction, making it less likely for DHG. This model was described for melittin, a much larger lytic molecule with a significantly different kinetic as observed in our experiments. Referring to the crystal structure of DHG with cation, we hypothesize that the shape can be reminiscent of a channel-like structure potentially fitting to the barrel stave model: di-keto units facing inwards and hydrophobic double bonds facing outwards. Structure-activity-relationships of the class indicate that both the double-bond backbone (C13-C20) and the di-keto unit are essential for activity.[11,12] We postulate that chlorotonils integrate into the membrane and interact hydrophobically with saturated acyl chains of membrane lipids, while the hydrophilic lactone orients toward polar head groups. It remains uncertain whether an actual channel is formed, similar to daptomycin or gramicidin,[53,54] or if binding results in conformational changes within the membrane. A single DHG monomer (12.4 Å in length) lacks the capacity to span the entire double-membrane (approx. 30 Å), hence, multiple molecules must converge to induce membrane depolarization if the MoA relies on pore formation.[54] Using mass spectrometry, we observed the formation of DHG-multimers together with sodium supporting this hypothesis (Figure 6A). Observed overexpression of staphylococcal complement inhibitor SCIN upon DHG treatment further fits this theory, as SCIN counteracts the formation of the membrane attack complex necessary for osmotic lysis of target pathogens.[55,56] As the increase in specific membrane capacitance can result from a decrease in membrane thickness, the interaction could be similar to Gramicidin, where two multimers converge together to form a channel while decreasing membrane thickness.[54] We hypothesize further that upon initial contact, the compound attaches to the bacterial membrane inducing depolarization and the VBNC-state. However, as long as the cell has enough energy left to adapt and to re-establish a functional membrane potential, non-inhibited regrowth is possible, which is also in line with our potassium-rescue experiments. We further also observed effects on peptidoglycan biosynthesis and potentially protein biosynthesis in form of YbjG and MetAP inhibition, complementing our current MoA analysis in bacteria (Figure 7). For *P. falciparum*, the fast-acting kinetic of chlorotonils was described previously,[57] however as shown here, the activity was not significantly influenced by altered Na^+/K^+-concentrations as described for bacteria and so far we could not observe significant effects on erythrocytes that might explain effects on intra-erythrocytic parasites. Neither were any similarities to cipargamin observed, a known sodium pump (PfATP4) targeting drug,[22,23] suggesting a different antiplasmodial mechanism.

Membrane-active antibiotics overcome resistances in clinical isolates that are conferred by e.g., target mutations or increased efflux; however, they might suffer from poor selectivity.[58–60] Previously, we have only screened against human HepG2 cells, as this model is most commonly used for *in vitro* toxicity studies. We found no effect, and we further found only minor developmental toxicity against zebrafish larvae (IC_{50} 27.4 μM).[11,12] Having confirmed binding of DHG also to eukaryotic lipid species, we extended cytological screening to additional cell lines revealing IC_{50}s in the single digit micromolar range for DHG, with HEK293 cells being the most

sensitive. In general, IC_{50}s even against sensitive cell lines were significantly higher (70- to 128-fold) than the nanomolar activity against bacterial cells and were all also above maximal serum concentrations of DHG in mice.[12] We have shown that potassium efflux could also be measured upon treatment of cell lines *in vitro*, generally confirming cross-species-reactivity of the compound class with a mechanism akin to the bacterial MoA. The available assay set up, however, does only allow for qualitative conclusions and only serves as proof-of-concept data, as the concentration used in our potassium-release assay was much higher than c_{max} in blood plasma.[12] Same for native-lipid MS, which also only delivers a qualitative answer for binding, rather than binding parameters that would allow to draw conclusions about selectivity between bacterial or eukaryotic lipids. Our main concern was a negative effect on erythrocytes and blood potassium concentrations; however, we could show that serum-relevant concentrations did not induce significant potassium-release from erythrocytes *in vitro*. Fortunately, we could then also confirm that the application of DHG at effective concentrations in mice for four consecutive days did not cause an increase in blood potassium concentration. We have previously shown that DHG was well tolerated in mouse infection models,[10–13] but we are aware that further studies are needed to assess *in vivo* tolerability to further de-risk the application of DHG especially in lights of its MoA. The potential for lipid/fatty acid selectivity should be assessed, but so far the *in vivo* tolerability seems only a result of low amount of free drug rather than a direct product of binding specificity/affinity. Further, positive charges of a DHG-cation complex should be considered as this was identified as a main driver of selectivity toward bacterial cells, as well as the influence of cholesterol in eukaryotic membranes, as this was shown to diminish effectiveness of membrane-active substances by significantly influencing permeability and accessibility of eukaryotic membranes.[59–62]

We conclude that with a suitable treatment regimen *in vivo*, safe and effective doses of DHG can be delivered, while resistance development might almost be impossible, as the fast-acting activity in combination with the complex mechanism of action makes DHG a highly effective antimicrobial agent and certainly a promising molecule for the development of a resistance breaking antibiotic.

Limitations of the study

Chlorotonils can target the cell wall biosynthesis through inhibiting YbjG, and while we also assessed MraY, MurG, and PBP2, the observed pentapeptide accumulation could potentially result from MurJ inhibition which we did not specifically test for. Furthermore, the selectivity and specificity of this compound class were not entirely evaluated in this study, hence, these aspects should be assessed in the future to provide compelling evidence of DHG's safety.

RESOURCE AVAILABILITY

Lead contact

Requests for further information and resources should be directed to and will be fulfilled by the lead contact Dr. Jennifer Herrmann (Jennifer.herrmann@helmholtz-hips.de)

Materials availability

This study did not generate new unique reagents.

Data and code availability

- Genomic data were deposited in the NCBI SRA database. Crystallographic information was deposited at the Cambridge Crystallographic Data Center and Fachinformationszentrum Karlsruhe. Original electron diffraction data of $Co[DHG]_3$ and further information are deposited at zenodo. Proteomics data have been deposited to the ProteomeXchange Consortium (PRIDE). All datasets are publicly available as of the date of publication. Accession numbers are listed in the key resources table.
- This paper does not report original code.
- Any additional information required to reanalyze the data reported in this paper is available from the lead contact upon request.

ACKNOWLEDGMENTS

The authors are grateful to Peer Lukat (SFPR, HZI) for his crystallization efforts, for collecting the synchrotron data of the Al DHG complex and for his support in the Coot refinement of Co DHG. We thank Anna-Lena Huber (MINS, HIPS) and Achim Biesel (DDEL, HIPS), for their help during RNA extraction and liposome preparation, respectively. We further thank Maren Scharfe and Doris Jaerke (Genome analytics, HZI) for genome sequencing, Ina Brentrop for EM sample preparation (ZEIM, HZI), and Alexandra Amann for cytotoxicity testing (MINS; HIPS) We gratefully acknowledge funding by the Federal Ministry of Education and Research (BMBF, 16GW0204K, ChloroClinaria), the German Center for Infection Research (DZIF, TTU-09.826 and TTU-09.923), and the Cluster of Excellence EXC2124 Controlling Microbes to Fight Infection (CMFI, project ID 390838134). The project was further supported by Pre4D funding of HZI.

AUTHOR CONTRIBUTIONS

Conceptualization: F.D., D.M., R.M., and Jennifer Hermann; Methodology: F.D., D.M., J.D., A.V., D.C.S., N.K., J.B., L.P.C., T.E.G., M.M., and M.B.; Validation: F.D., D.M., J.D., A.V., D.C.S., N.K., J.B., L.P.C., M.B., T.E.G., C.K., T.R., and M.M.; Formal Analysis: F.D., D.M., J.D., A.V., J.B.; Investigation: F.D., D.M., J.D., A.V., D.C.S., N.K., J.B., L.P.C., M.B., T.E.G., C.K., T.R., L.H.B., A.A., and M.M.; Data curation: F.D., Jennifer Hermann; Writing – original draft: F.D. and D.M., Jennifer Hermann; Writing – review and editing: F.D., A.M.K., Jana Held, R.S., M.B., H.B., T.S., S.S., R.M., Jennifer Hermann; Visualization: F.D., D.M., J.D., and A.V.; Project administration: F.D., A.M.K., R.M., and Jennifer Hermann; Funding acquisition: F.D., A.M.K., Jana Held, H.B., R.M., and Jennifer Hermann; Software programming: F.P.J.H.;Resources: G.J., W.H., M.B., R.S., H.B., T.S., S.S., and R.M.; Supervision: A.M.K., Jana-Held, M.B., R.S., H.B., T.S., S.S., R.M., and Jennifer Hermann.

DECLARATION OF INTERESTS

The authors declare that they are holders of a patent (WO2019/092030) and a pending patent application (PCT/EP2024/067834) that protect chlorotonils and further derivatives, including DHG. S.S. and R.M. are part of the advisory board of the journal.

STAR★METHODS

Detailed methods are provided in the online version of this paper and include the following:

- KEY RESOURCES TABLE
- EXPERIMENTAL MODEL AND STUDY PARTICIPANT DETAILS
  - Microbe strains
  - Cell lines
  - Animal studies
- METHOD DETAILS
  - Experimental compounds
  - Susceptibility assays

- Growth analyses
- Time-kill-kinetics
- Electron microscopy
- Propidium iodide stain
- FM5-95
- Induction of lia-lux cell wall stress response
- B. subtilis lacZ bioreporter agar assay
- UDP-Mur*NA*c pentapeptide accumulation
- MurG activity assay
- YbjG inhibition
- Microscale thermophoresis
- Membrane depolarisation
- *B. subtilis* minD delocalization study
- Potassium selective electrode
- ICP-MS measurements
- Maintenance of Plasmodium asexual stages
- Growth inhibition assays with asexual parasites
- Full proteome analysis
- Thermal proteome profiling
- Cloning and expression of *S. aureus* MetAP
- *Sa*MetAP activity assay
- Crystal structure
- Resistance generation and sequencing
- RNA extraction and quantitative PCR
- Lipid experiments
- Lipid membrane formation in microfluidics
- Determination of dehalogenil blood concentrations

- QUANTIFICATION AND STATISTICAL ANALYSIS

SUPPLEMENTAL INFORMATION

Supplemental information can be found online at https://doi.org/10.1016/j.chembiol.2025.03.005.

Received: August 21, 2024
Revised: December 12, 2024
Accepted: March 18, 2025
Published: April 8, 2025

REFERENCES

1. Murray, C.J., Ikuta, K.S., Sharara, F., Swetschinski, L., Robles Aguilar, G., Gray, A., Han, C., Bisignano, C., Rao, P., Wool, E., et al. (2022). Global burden of bacterial antimicrobial resistance in 2019: a systematic analysis. Lancet (London, England) *399*, 629–655. https://doi.org/10.1016/S0140-6736(21)02724-0.
2. O'Neill, J. (2014). Antimicrobial Resistance: Tackling a Crisis for the Health and Wealth of Nations (Elsevier Ltd). https://doi.org/10.1016/J.JCLEPRO.2022.130949.
3. Outterson, K. (2021). Estimating The Appropriate Size Of Global Pull Incentives For Antibacterial Medicines. Health Aff. *40*, 1758–1765. https://doi.org/10.1377/HLTHAFF.2021.00688.
4. Shlaes, D.M. (2019). The economic conundrum for antibacterial drugs. Antimicrob. Agents Chemother. *64*, e02057-19. https://doi.org/10.1128/aac.02057-19.
5. World Health Organization (2024). 2023 Antibacterial agents in clinical and preclinical development an overview and analysis, pp. 1–231.
6. Butler, M.S., Henderson, I.R., Capon, R.J., and Blaskovich, M.A.T. (2023). Antibiotics in the clinical pipeline as of December 2022. J. Antibiot. *76*, 431–473. https://doi.org/10.1038/s41429-023-00629-8.
7. WHO (2017). WHO | Prioritization of pathogens to guide discovery, research and development of new antibiotics for drug resistant bacterial infections, Including Tuberculosis (WHO).
8. World Health Organization (2024). WHO bacterial priority pathogens list, 2024: bacterial pathogens of public health importance, to guide research, development and strategies to prevent and control antimicrobial resistance (World Health Organization).
9. Newman, D.J., and Cragg, G.M. (2020). Natural Products as Sources of New Drugs over the Nearly Four Decades from 01/1981 to 09/2019. J. Nat. Prod. *83*, 770–803.
10. Held, J., Gebru, T., Kalesse, M., Jansen, R., Gerth, K., Müller, R., and Mordmüller, B. (2014). Antimalarial Activity of the Myxobacterial Macrolide Chlorotonil A. Antimicrob. Agents Chemother. *58*, 6378–6384. https://doi.org/10.1128/AAC.03326-14.
11. Hofer, W., Oueis, E., Fayad, A.A., Deschner, F., Andreas, A., de Carvalho, L.P., Hüttel, S., Bernecker, S., Pätzold, L., Morgenstern, B., et al. (2022). Regio- and Stereoselective Epoxidation and Acidic Epoxide Opening of Antibacterial and Antiplasmodial Chlorotonils Yield Highly Potent Derivatives. Angew. Chem. Int. Ed. Engl. *61*, e202202816. https://doi.org/10.1002/ANIE.202202816.
12. Hofer, W., Deschner, F., Jézéquel, G., Pessanha de Carvalho, L., Abdel-Wadood, N., Pätzold, L., Bernecker, S., Morgenstern, B., Kany, A.M., Große, M., et al. (2024). Functionalization of Chlorotonils: Dehalogenil as Promising Lead Compound for In Vivo Application. Angew. Chemie Int. Ed. *63*, e202319765. https://doi.org/10.1002/ANIE.202319765.
13. Bublitz, A., Brauer, M., Wagner, S., Hofer, W., Müsken, M., Deschner, F., Lesker, T.R., Neumann-Schaal, M., Paul, L.S., Nübel, U., et al. (2023). The natural product chlorotonil A preserves colonization resistance and prevents relapsing Clostridioides difficile infection. Cell Host Microbe *31*, 734–750.e8. https://doi.org/10.1016/J.CHOM.2023.04.003.
14. Davison, E.K., Freeman, J.L., Zhang, W., Wuest, W.M., Furkert, D.P., and Brimble, M.A. (2020). Asymmetric Total Synthesis of the Naturally Occurring Antibiotic Anthracimycin. Org. Lett. *22*, 5550–5554. https://doi.org/10.1021/acs.orglett.0c01913.
15. Hensler, M.E., Jang, K.H., Thienphrapa, W., Vuong, L., Tran, D.N., Soubih, E., Lin, L., Haste, N.M., Cunningham, M.L., Kwan, B.P., et al. (2014). Anthracimycin activity against contemporary methicillin-resistant Staphylococcus aureus. J. Antibiot. *67*, 549–553. https://doi.org/10.1038/JA.2014.36.
16. Jungmann, K., Jansen, R., Gerth, K., Huch, V., Krug, D., Fenical, W., and Müller, R. (2015). Two of a Kind–The Biosynthetic Pathways of Chlorotonil and Anthracimycin. ACS Chem. Biol. *10*, 2480–2490. https://doi.org/10.1021/ACSCHEMBIO.5B00523.
17. Mascher, T., Zimmer, S.L., Smith, T.-A., and Helmann, J.D. (2004). Antibiotic-Inducible Promoter Regulated by the Cell Envelope Stress-Sensing Two-Component System LiaRS of Bacillus subtilis. Antimicrob. Agents Chemother. *48*, 2888–2896. https://doi.org/10.1128/AAC.48.8.2888-2896.2004.
18. Schneider, T., Gries, K., Josten, M., Wiedemann, I., Pelzer, S., Labischinski, H., and Sahl, H.G. (2009). The lipopeptide antibiotic Friulimicin B inhibits cell wall biosynthesis through complex formation with bactoprenol phosphate. Antimicrob. Agents Chemother. *53*, 1610–1618. https://doi.org/10.1128/AAC.01040-08.
19. TouzÉ, T., and Mengin-Lecreulx, D. (2008). Undecaprenyl Phosphate Synthesis. EcoSal Plus *3*, 1–20. https://doi.org/10.1128/ECOSALPLUS.4.7.1.7.
20. Workman, S.D., Worrall, L.J., and Strynadka, N.C.J. (2018). Crystal structure of an intramembranal phosphatase central to bacterial cell-wall peptidoglycan biosynthesis and lipid recycling. Nat. Commun. *9*, 1159. https://doi.org/10.1038/s41467-018-03547-8.
21. Strahl, H., and Hamoen, L.W. (2010). Membrane potential is important for bacterial cell division. Proc. Natl. Acad. Sci. USA *107*, 12281–12286. https://doi.org/10.1073/PNAS.1005485107.
22. Bouwman, S.A., Zoleko-Manego, R., Renner, K.C., Schmitt, E.K., Mombo-Ngoma, G., and Grobusch, M.P. (2020). The early preclinical and clinical development of cipargamin (KAE609), a novel antimalarial compound. Travel Med. Infect. Dis. *36*, 101765. https://doi.org/10.1016/j.tmaid.2020.101765.
23. Spillman, N.J., Allen, R.J.W., McNamara, C.W., Yeung, B.K.S., Winzeler, E.A., Diagana, T.T., and Kirk, K. (2013). Na+ Regulation in the Malaria

Parasite Plasmodium falciparum Involves the Cation ATPase PfATP4 and Is a Target of the Spiroindolone Antimalarials. Cell Host Microbe *13*, 227–237. https://doi.org/10.1016/j.chom.2012.12.006.

24. Franken, H., Mathieson, T., Childs, D., Sweetman, G.M.A., Werner, T., Tögel, I., Doce, C., Gade, S., Bantscheff, M., Drewes, G., et al. (2015). Thermal proteome profiling for unbiased identification of direct and indirect drug targets using multiplexed quantitative mass spectrometry. Nat. Protoc. *1010*, 1567–1593. https://doi.org/10.1038/nprot.2015.101.
25. Mateus, A., Määttä, T.A., and Savitski, M.M. (2017). Thermal proteome profiling: Unbiased assessment of protein state through heat-induced stability changes. Proteome Sci. *15*, 1–7. https://doi.org/10.1186/s12953-017-0122-4.
26. Childs, D., Bach, K., Franken, H., Anders, S., Kurzawa, N., Bantscheff, M., Savitski, M.M., and Huber, W. (2019). Nonparametric Analysis of Thermal Proteome Profiles Reveals Novel Drug-binding Proteins. Mol. Cell. Proteomics *18*, 2506–2515. https://doi.org/10.1074/MCP.TIR119.001481.
27. Gaballa, A., Newton, G.L., Antelmann, H., Parsonage, D., Upton, H., Rawat, M., Claiborne, A., Fahey, R.C., and Helmann, J.D. (2010). Biosynthesis and functions of bacillithiol, a major low-molecular-weight thiol in Bacilli. Proc. Natl. Acad. Sci. USA *107*, 6482–6486. https://doi.org/10.1073/PNAS.1000928107.
28. Lowther, W.T., and Matthews, B.W. (2000). Structure and function of the methionine aminopeptidases. Biochim. Biophys. *1477*, 157–167. https://doi.org/10.1016/s0167-4838(99)00271-x.
29. Kishor, C., Gumpena, R., Reddi, R., and Addlagatta, A. (2012). Structural studies of Enterococcus faecalis methionine aminopeptidase and design of microbe specific 2,2′-bipyridine based inhibitors. Medchemcomm *3*, 1406–1412. https://doi.org/10.1039/C2MD20096A.
30. Oefner, C., Douangamath, A., D'Arcy, A., Häfeli, S., Mareque, D., Mac Sweeney, A., Padilla, J., Pierau, S., Schulz, H., Thormann, M., et al. (2003). The 1.15 Å Crystal Structure of the Staphylococcus aureus Methionyl-aminopeptidase and Complexes with Triazole Based Inhibitors. J. Mol. Biol. *332*, 13–21. https://doi.org/10.1016/S0022-2836(03)00862-3.
31. Deschner, F., Risch, T., Baier, C., Schlüter, D., Herrmann, J., and Müller, R. (2024). Nitroxoline resistance is associated with significant fitness loss and diminishes in vivo virulence of Escherichia coli. Microbiol. Spectr. *12*, e0307923. https://doi.org/10.1128/spectrum.03079-23.
32. Huang, L., Matsuo, M., Calderón, C., Fan, S.H., Ammanath, A.V., Fu, X., Li, N., Luqman, A., Ullrich, M., Herrmann, F., et al. (2022). Molecular Basis of Rhodomyrtone Resistance in Staphylococcus aureus. mBio *13*, e03833-21. https://doi.org/10.1128/MBIO.03833-21.
33. Saising, J., Nguyen, M.T., Härtner, T., Ebner, P., Al Mamun Bhuyan, A., Berscheid, A., Muehlenkamp, M., Schäkermann, S., Kumari, N., Maier, M.E., et al. (2018). Rhodomyrtone (Rom) is a membrane-active compound. Biochim. Biophys. Acta. Biomembr. *1860*, 1114–1124. https://doi.org/10.1016/J.BBAMEM.2018.01.011.
34. Rahn, N., and Kalesse, M. (2008). The Total Synthesis of Chlorotonil A. Angew. Chem. Int. Ed. Engl. *47*, 597–599. https://doi.org/10.1002/ANIE.200703930.
35. Brogden, K.A. (2005). Antimicrobial peptides: pore formers or metabolic inhibitors in bacteria? Nat. Rev. Microbiol. *3*, 238–250. https://doi.org/10.1038/nrmicro1098.
36. Yeaman, M.R., and Yount, N.Y. (2003). Mechanisms of Antimicrobial Peptide Action and Resistance. Pharmacol. Rev. *55*, 27–55. https://doi.org/10.1124/PR.55.1.2.
37. Benarroch, J.M., and Asally, M. (2020). The Microbiologist's Guide to Membrane Potential Dynamics at (Elsevier Ltd). https://doi.org/10.1016/j.tim.2019.12.008.
38. Helgren, T.R., Wangtrakuldee, P., Staker, B.L., and Hagen, T.J. (2016). Advances in Bacterial Methionine Aminopeptidase Inhibition. Curr. Top. Med. Chem. *16*, 397–414. https://doi.org/10.2174/1568026615666150813145410.
39. Mateus, A., Kurzawa, N., Becher, I., Sridharan, S., Helm, D., Stein, F., Typas, A., and Savitski, M.M. (2020). Thermal proteome profiling for interrogating protein interactions. Mol. Syst. Biol. *16*, 9232. https://doi.org/10.15252/msb.20199232.
40. Sridharan, S., Kurzawa, N., Werner, T., Günthner, I., Helm, D., Huber, W., Bantscheff, M., and Savitski, M.M. (2019). Proteome-wide solubility and thermal stability profiling reveals distinct regulatory roles for ATP. Nat. Commun. *101*, 1155. https://doi.org/10.1038/s41467-019-09107-y.
41. Jarzab, A., Kurzawa, N., Hopf, T., Moerch, M., Zecha, J., Leijten, N., Bian, Y., Musiol, E., Maschberger, M., Stoehr, G., et al. (2020). Meltome atlas—thermal proteome stability across the tree of life. Nat. Methods *175*, 495–503. https://doi.org/10.1038/s41592-020-0801-4.
42. Sukharev, S., and Anishkin, A. (2022). Mechanosensitive Channels: History, Diversity, and Mechanisms. Biochem. (Moscow), Suppl. Ser. A Membr. Cell Biol. *164*, 291–310. https://doi.org/10.1134/S1990747822090021.
43. Li, Y., Moe, P.C., Chandrasekaran, S., Booth, I.R., and Blount, P. (2002). Ionic regulation of MscK, a mechanosensitive channel from Escherichia coli. EMBO J. *21*, 5323–5330. https://doi.org/10.1093/EMBOJ/CDF537.
44. Saeloh, D., Tipmanee, V., Jim, K.K., Dekker, M.P., Bitter, W., Voravuthikunchai, S.P., Wenzel, M., and Hamoen, L.W. (2018). The novel antibiotic rhodomyrtone traps membrane proteins in vesicles with increased fluidity. PLoS Pathog. *14*, e1006876. https://doi.org/10.1371/journal.ppat.1006876.
45. Fuchs, S., Mehlan, H., Bernhardt, J., Hennig, A., Michalik, S., Surmann, K., Pané-Farré, J., Giese, A., Weiss, S., Backert, L., et al. (2018). AureoWiki - The repository of the Staphylococcus aureus research and annotation community. Int. J. Med. Microbiol. *308*, 558–568. https://doi.org/10.1016/J.IJMM.2017.11.011.
46. MacDermott-Opeskin, H.I., Gupta, V., and O'Mara, M.L. (2022). Lipid-mediated antimicrobial resistance: a phantom menace or a new hope? Biophys. Rev. *14*, 145–162. https://doi.org/10.1007/S12551-021-00912-8.
47. Pader, V., Hakim, S., Painter, K.L., Wigneshweraraj, S., Clarke, T.B., and Edwards, A.M. (2016). Staphylococcus aureus inactivates daptomycin by releasing membrane phospholipids. Nat. Microbiol. *2*, 16194–16198. https://doi.org/10.1038/nmicrobiol.2016.194.
48. Andries, K., Villellas, C., Coeck, N., Thys, K., Gevers, T., Vranckx, L., Lounis, N., De Jong, B.C., and Koul, A. (2014). Acquired resistance of Mycobacterium tuberculosis to bedaquiline. PLoS One *9*, e102135. https://doi.org/10.1371/JOURNAL.PONE.0102135.
49. Li, L., Abdelhady, W., Donegan, N.P., Seidl, K., Cheung, A., Zhou, Y.F., Yeaman, M.R., Bayer, A.S., and Xiong, Y.Q. (2018). Role of Purine Biosynthesis in Persistent Methicillin-Resistant Staphylococcus aureus Infection. J. Infect. Dis. *218*, 1367–1377. https://doi.org/10.1093/INFDIS/JIY340.
50. Warsi, O.M., Upterworth, L.M., Breidenstein, A., Lustig, U., Mikkelsen, K., Nagy, T., Szatmari, D., Ingmer, H., and Andersson, D.I. (2024). Staphylococcus aureus mutants resistant to the feed-additive monensin show increased virulence and altered purine metabolism. mBio *15*, e0315523. https://doi.org/10.1128/MBIO.03155-23.
51. Dave, U.C., and Kadeppagari, R.K. (2019). Alanine dehydrogenase and its applications - A review. Crit. Rev. Biotechnol. *39*, 648–664. https://doi.org/10.1080/07388551.2019.1594153.
52. Molenaar, D., Van Der Rest, M.E., and Petrović, S. (1998). Biochemical and genetic characterization of the membrane-associated malate dehydrogenase (acceptor) from Corynebacterium glutamicum. Eur. J. Biochem. *254*, 395–403. https://doi.org/10.1046/J.1432-1327.1998.2540395.X.
53. Taylor, S.D., and Palmer, M. (2016). The action mechanism of daptomycin. Bioorg. Med. Chem. *24*, 6253–6268. https://doi.org/10.1016/J.BMC.2016.05.052.
54. Jensen, M.R., and Freeman, M.F. (2020). Structure and Biosynthesis of Proteusin RiPP Natural Products. Compr. Nat. Prod. *III*, 88–118. https://doi.org/10.1016/B978-0-12-409547-2.14727-4.
55. Rooijakkers, S.H.M., Wu, J., Ruyken, M., van Domselaar, R., Planken, K.L., Tzekou, A., Ricklin, D., Lambris, J.D., Janssen, B.J.C., van Strijp,

J.A.G., and Gros, P. (2009). Structural and functional implications of the alternative complement pathway C3 convertase stabilized by a staphylococcal inhibitor. Nat. Immunol. *107*, 721–727. https://doi.org/10.1038/ni.1756.

56. Xie, C.B., Jane-Wit, D., and Pober, J.S. (2020). Complement Membrane Attack Complex: New Roles, Mechanisms of Action, and Therapeutic Targets. Am. J. Pathol. *190*, 1138–1150. https://doi.org/10.1016/J.AJPATH.2020.02.006.

57. de Carvalho, L.P., Niepoth, E., Mavraj-Husejni, A., Kreidenweiss, A., Herrmann, J., Müller, R., Knaab, T., Burckhardt, B.B., Kurz, T., and Held, J. (2023). Quantification of Plasmodium falciparum HRP-2 as an alternative method to [3H]hypoxanthine incorporation to measure the parasite reduction ratio in vitro. Int. J. Antimicrob. Agents *62*, 106894. https://doi.org/10.1016/J.IJANTIMICAG.2023.106894.

58. Hurdle, J.G., O'Neill, A.J., Chopra, I., and Lee, R.E. (2011). Targeting bacterial membrane function: an underexploited mechanism for treating persistent infections. Nat. Rev. Microbiol. *9*, 62–75. https://doi.org/10.1038/NRMICRO2474.

59. Zhang, N., and Ma, S. (2019). Recent development of membrane-active molecules as antibacterial agents. Eur. J. Med. Chem. *184*, 111743. https://doi.org/10.1016/J.EJMECH.2019.111743.

60. Mingeot-Leclercq, M.-P., and Décout, J.-L. (2016). Bacterial lipid membranes as promising targets to fight antimicrobial resistance, molecular foundations and illustration through the renewal of aminoglycoside antibiotics and emergence of amphiphilic aminoglycosides. Medchemcomm *7*, 586–611. https://doi.org/10.1039/C5MD00503E.

61. Brender, J.R., McHenry, A.J., and Ramamoorthy, A. (2012). Does cholesterol play a role in the bacterial selectivity of antimicrobial peptides? Front. Immunol. *3*, 31501. https://doi.org/10.3389/FIMMU.2012.00195/BIBTEX.

62. Ali, O., and Szabó, A. (2023). Review of Eukaryote Cellular Membrane Lipid Composition, with Special Attention to the Fatty Acids. Int. J. Mol. Sci. *24*, 15693. https://doi.org/10.3390/IJMS242115693.

63. Sekyere, J.O., and Amoako, D.G. (2017). Carbonyl Cyanide m-Chlorophenylhydrazine (CCCP) Reverses Resistance to Colistin, but Not to Carbapenems and Tigecycline in Multidrug-Resistant Enterobacteriaceae. Front. Microbiol. *8*, 228. https://doi.org/10.3389/FMICB.2017.00228.

64. Ducret, A., Quardokus, E.M., and Brun, Y.V. (2016). MicrobeJ, a tool for high throughput bacterial cell detection and quantitative analysis. Nat. Microbiol. *1*, 16077. https://doi.org/10.1038/nmicrobiol.2016.77.

65. Zhang, L., Esquembre, L.A., Xia, S.N., Oesterhelt, F., Hughes, C.C., Brötz-Oesterhelt, H., and Teufel, R. (2022). Antibacterial Synnepyrroles from Human-Associated Nocardiopsis sp. Show Protonophore Activity and Disrupt the Bacterial Cytoplasmic Membrane. ACS Chem. Biol. *17*, 2836–2848. https://doi.org/10.1021/ACSCHEMBIO.2C00460.

66. Tan, S., Ludwig, K.C., Müller, A., Schneider, T., and Nodwell, J.R. (2019). The Lasso Peptide Siamycin-I Targets Lipid II at the Gram-Positive Cell Surface. ACS Chem. Biol. *14*, 966–974. https://doi.org/10.1021/ACSCHEMBIO.9B00157.

67. Radeck, J., Gebhard, S., Orchard, P.S., Kirchner, M., Bauer, S., Mascher, T., and Fritz, G. (2016). Anatomy of the bacitracin resistance network in Bacillus subtilis. Mol. Microbiol. *100*, 607–620. https://doi.org/10.1111/mmi.13336.

68. Wex, K.W., Saur, J.S., Handel, F., Ortlieb, N., Mokeev, V., Kulik, A., Niedermeyer, T.H.J., Mast, Y., Grond, S., Berscheid, A., and Brötz-Oesterhelt, H. (2021). Bioreporters for direct mode of action-informed screening of antibiotic producer strains. Cell Chem. Biol. *28*, 1242–1252.e4. https://doi.org/10.1016/j.chembiol.2021.02.022.

69. Stulke, J., Hanschke, R., and Hecker, M. (1993). Temporal activation of -glucanase synthesis in Bacillus subtilis is mediated by the GTP pool. J. Gen. Microbiol. *139*, 2041–2045. https://doi.org/10.1099/00221287-139-9-2041.

70. Herbert, S., Ziebandt, A.-K., Ohlsen, K., Schäfer, T., Hecker, M., Albrecht, D., Novick, R., and Götz, F. (2010). Repair of Global Regulators in Staphylococcus aureus 8325 and Comparative Analysis with Other Clinical Isolates. Infect. Immun. *78*, 2877–2889. https://doi.org/10.1128/IAI.00088-10.

71. Mann, P.A., Müller, A., Xiao, L., Pereira, P.M., Yang, C., Ho Lee, S., Wang, H., Trzeciak, J., Schneeweis, J., dos Santos, M.M., et al. (2013). Murgocil is a Highly Bioactive Staphylococcal-Specific Inhibitor of the Peptidoglycan Glycosyltransferase Enzyme MurG. ACS Chem. Biol. *8*, 2442–2451. https://doi.org/10.1021/cb400487f.

72. Ling, L.L., Schneider, T., Peoples, A.J., Spoering, A.L., Engels, I., Conlon, B.P., Mueller, A., Schäberle, T.F., Hughes, D.E., Epstein, S., et al. (2015). A new antibiotic kills pathogens without detectable resistance. Nature *517*, 455–459. https://doi.org/10.1038/NATURE14098.

73. Marston, A.L., Thomaides, H.B., Edwards, D.H., Sharpe, M.E., and Errington, J. (1998). Polar localization of the MinD protein of Bacillus subtilis and its role in selection of the mid-cell division site. Genes Dev. *12*, 3419–3430. https://doi.org/10.1101/GAD.12.21.3419.

74. Otten, C., De Benedetti, S., Gaballah, A., Bühl, H., Klöckner, A., Brauner, J., Sahl, H.G., and Henrichfreise, B. (2015). Co-Solvents as Stabilizing Agents during Heterologous Overexpression in Escherichia coli – Application to Chlamydial Penicillin-Binding Protein 6. PLoS One *10*, e0122110. https://doi.org/10.1371/JOURNAL.PONE.0122110.

75. Schneider, C.A., Rasband, W.S., and Eliceiri, K.W. (2012). NIH Image to ImageJ: 25 years of image analysis. Nat. Methods *9*, 671–675. https://doi.org/10.1038/nmeth.2089.

76. Orlov, D.S., Nguyen, T., and Lehrer, R.I. (2002). Potassium release, a useful tool for studying antimicrobial peptides. J. Microbiol. Methods *49*, 325–328. https://doi.org/10.1016/S0167-7012(01)00383-9.

77. De Carvalho, L.P., Sandri, T.L., Tenório de Melo, E.J., Fendel, R., Kremsner, P.G., Mordmüller, B., and Held, J. (2019). Ivermectin impairs the development of sexual and asexual stages of plasmodium falciparum in vitro. Antimicrob. Agents Chemother. *63*, e00085-19. https://doi.org/10.1128/AAC.00085-19.

78. Trager, W., and Jensen, J.B. (1976). Human Malaria Parasites in Continuous Culture. Science *193*, 673–675. https://doi.org/10.1126/science.781840.

79. Noedl, H., Bronnert, J., Yingyuen, K., Attlmayr, B., Kollaritsch, H., and Fukuda, M. (2005). Simple Histidine-Rich Protein 2 Double-Site Sandwich Enzyme-Linked Immunosorbent Assay for Use in Malaria Drug Sensitivity Testing. Antimicrob. Agents Chemother. *49*, 3575–3577. https://doi.org/10.1128/AAC.49.8.3575-3577.2005.

80. de Carvalho, L.P., Groeger-Otero, S., Kreidenweiss, A., Kremsner, P.G., Mordmüller, B., and Held, J. (2021). Boromycin has Rapid-Onset Antibiotic Activity Against Asexual and Sexual Blood Stages of Plasmodium falciparum. Front. Cell. Infect. Microbiol. *11*, 802294. https://doi.org/10.3389/fcimb.2021.802294.

81. Ritz, C., Baty, F., Streibig, J.C., and Gerhard, D. (2015). Dose-Response Analysis Using R. PLoS One *10*, e0146021. https://doi.org/10.1371/journal.pone.0146021.

82. Demichev, V., Messner, C.B., Vernardis, S.I., Lilley, K.S., and Ralser, M. (2020). DIA-NN: neural networks and interference correction enable deep proteome coverage in high throughput. Nat. Methods *17*, 41–44. https://doi.org/10.1038/s41592-019-0638-x.

83. Tyanova, S., Temu, T., Sinitcyn, P., Carlson, A., Hein, M.Y., Geiger, T., Mann, M., and Cox, J. (2016). The Perseus computational platform for comprehensive analysis of (prote)omics data. Nat. Methods *13*, 731–740. https://doi.org/10.1038/nmeth.3901.

84. Hu, Y., Mostert, D., Orgler, C., Andler, O., Zischka, H., Kazmaier, U., Vollmar, A.M., Braig, S., Sieber, S.A., and Zahler, S. (2024). Thermal Proteome Profiling Reveals Insight to Antiproliferative and Pro-Apoptotic Effects of Lagunamide A in the Modulation of DNA Damage Repair. Chembiochem *25*, e202400024. https://doi.org/10.1002/CBIC.202400024.

85. Cox, J., and Mann, M. (2008). MaxQuant enables high peptide identification rates, individualized p.p.b.-range mass accuracies and proteome-wide protein quantification. Nat. Biotechnol. *2612*, 1367–1372. https://doi.org/10.1038/nbt.1511.

86. Sheldrick, G.M. (2015). SHELXT – Integrated space-group and crystal-structure determination. Acta Crystallogr. A Found. Adv. *71*, 3–8. https://doi.org/10.1107/S2053273314026370.

87. Sheldrick, G.M. (2015). Crystal structure refinement with SHELXL. Acta Crystallogr. C Struct. Chem. *71*, 3–8. https://doi.org/10.1107/S2053229614024218.

88. Vonrhein, C., Flensburg, C., Keller, P., Sharff, A., Smart, O., Paciorek, W., Womack, T., and Bricogne, G. (2011). Data processing and analysis with the autoPROC toolbox. Acta Crystallogr. D Biol. Crystallogr. *67*, 293–302. https://doi.org/10.1107/S0907444911007773.

89. McCoy, A.J., Grosse-Kunstleve, R.W., Adams, P.D., Winn, M.D., Storoni, L.C., and Read, R.J. (2007). Phaser crystallographic software. J. Appl. Crystallogr. *40*, 658–674. https://doi.org/10.1107/S0021889807021206.

90. Welti, R., Li, W., Li, M., Sang, Y., Biesiada, H., Zhou, H.-E., Rajashekar, C.B., Williams, T.D., and Wang, X. (2002). Profiling Membrane Lipids in Plant Stress Responses ROLE OF PHOSPHOLIPASE D IN FREEZING-INDUCED LIPID CHANGES IN ARABIDOPSIS. J. Biol. Chem. *277*, 31994–32002. https://doi.org/10.1074/jbc.M205375200.

91. Khangholi, N., Seemann, R., and Fleury, J.-B. (2020). Simultaneous measurement of surface and bilayer tension in a microfluidic chip. Biomicrofluidics *14*, 024117. https://doi.org/10.1063/1.5137810.

STAR★METHODS

KEY RESOURCES TABLE

REAGENT or RESOURCE	SOURCE	IDENTIFIER
Antibodies		
anti-Plasmodium falciparum HRP2 Antibody (Mouse IgM) - Monoclonal	ICLLAB	MPFM-55A; RRID: AB_831665
anti-Plasmodium falciparum HRPII Antibody (Mouse) - HRP Conjugated	ICLLAB	MPFG-55P; RRID: AB_777328
Bacterial and virus strains		
Staphylococcus aureus	ATCC	ATCC 29213
Escherichia coli ATCC25922	ATCC	ATCC 25922
B. subtilis 168 trpC2	Laboratory Stock	N/A
B. subtilis 1S34 P_{yorB}-*lacZ*	Wex et al. 2021	N/A
B. subtilis 1S34 P_{yppS}-*lacZ*	Wex et al. 2021	N/A
B. subtilis 1S34 P_{bmrC}-*lacZ*	Wex et al. 2021	N/A
B. subtilis 1S34 P_{ypuA}-*lacZ*	Wex et al. 2021	N/A
B. subtilis P_{lial}-*lux*	Radeck et al. 2016	N/A
B. subtilis gfp-minD	Marston et al. 1998	N/A
S. aureus HG001	Herbert et al. 2010	N/A
Plasmodium falciparum 3D7 strain	BEI resources	MRA-102
Plasmodium falciparum Dd2 strain	BEI resources	MRA-150
Plasmodium falciparum Dd2_SJ557733	Dr. David Fidock, Columbia University, NY	N/A
Biological samples		
Human Blood	Transfusion Center – University Hospital Tübingen	N/A
Chemicals, peptides, and recombinant proteins		
Chlorotonil A	Hofer et al., 2024	ChA
ChB1-Epo2	Hofer et al., 2024	ChB1-Epo2
Dehalogenil	Hofer et al., 2024	DHG WH0232J
Glutaraldehyde	Agar Scientific	Cat# R1010
Paraformaldehyde	Roth	0335.3
HEPES	Roth	9105.4
Sucrose	Sigma Aldrich	16104
CaCl2	Merck	2382
MgCl2	Merck	5833
NaCl	Fluka	Cat# 38979
KCl	Merck	Cat# 5002 (Discontinued)
KCl	Sigma-Aldrich	7447-40-7
Osmium tetroxide	Roth	8371.3
Ethanol	J.T. Baker	8025
Ethanol, Rotipuran	Roth	9065.2
Uranyl acetate	Electron Microscopy Sciences	#22400
LR White resin, catalyzed	Agar Scientific	AGR1280
LR White activator	Agar Scientific	AGR1283
gelatine capsules	Plano GmbH	G29202
Lead citrate ultrastain 2	Leica	705530
Pol-L-lysine	Sigma	P8920
Tris (Trizma Base)	Sigma	T-1503

(*Continued on next page*)

Continued

REAGENT or RESOURCE	SOURCE	IDENTIFIER
HCl	Roth	K025.1
EDTA	Sigma	No number
Acetone	J.T. Baker	8002
Acetone, Rotisolv	Roth	7328.2
Agar-Agar, Kobe I	Carl Roth	Cat# 5210.2
Agarose, low EEO	Fisher bioreagents	Cat# BP160-100
Dimethyl sulfoxide	Fisher bioreagents	Cat# D/4120/PB17
Dulbecco's phosphate buffered saline (DPBS) + $CaCl_2$ + $MgCl_2$	gibco™	Cat# 14040-091
Glucose	Sigma-Aldrich	Cat# 16301
Magnesium chloride heptahydrate	AppliChem	Cat# 131404
CCCP	Sigma-Aldrich	Cat# C2759
Nisin	Sigma-Aldrich	Cat# 5764
Oxoid™ ciprofloxacin (5 μg)	ThermoFisher Scientific	Cat# CT0425B
Oxoid™ rifampicin (40 μg)	ThermoFisher Scientific	Cat# CT0104B
Oxoid™ chloramphenicol (10 μg)	ThermoFisher Scientific	Cat# CT0012B
Oxoid™ vancomycin (30 μg)	ThermoFisher Scientific	Cat# CT0058B
Chloramphenicol	Roth	Cat# 3886.1
Vancomycin hydrochloride	Sigma-Aldrich	V2002
Chloroquine	Sigma-Aldrich	C6628
FM5-95	InvitrogenTM	Cat# T24460
DiOC2(3)	Molecular Probes	Cat# 14730
Ion strength adjuster	Mettler Toledo	51344762
Potassium standard	Mettler Toledo	51344777
Nitric acid	Roth	Cat# HN50.3
Hydrochloric acid	Roth	Cat# HN53.1
Beryllium standard	Agilent	Cat# G1820-65236
Triton X-100	Perkin Elmer	N9300260
n-butanol	Fischer Scientific	Cat# 11387946
Pyridinacetate	Merck	Cat# 1097280500
H3PO4	Sigma	Cat# 49685
Undecaprenyl-MPDA monophosphate $(NH_4^+)_2$	Larodan	62–1055
Undecaprenyl-DPTA diphosphate $(NH_4^+)_3$	Larodan	68–1100
Isopropanol	VWR	Cat# 9095.2500
Ammonia	Sigma-Aldrich	Cat# 392685
Chloroform	VWR	Cat# 83627.320
Lysyl Endopeptidase	Wako	Cat# 125-05061
Trypsin, Sequencing grade	Promega	Cat# V5111
BTTAA ligand	Sigma-Aldrich	Cat# 678937
Formic acid	Honeqwell	CAT# 94318-250-ML
ESI-L low-concentration tuning mix	Agilent	CAT# 1969-85000
Caesium iodide 99.9%	Thermo Fisher Scientific	CAT# 192050250
AlbuMax II	Gibco	11021029
Gentamycin	Sigma-Aldrich	G1264
Hypoxanthine	Sigma-Aldrich	H9377
Lysostaphin from *Staphylococcus staphylolyticus*	Sigma-Aldrich	L7386
RNAse A (DNAse free)	AppliChem	A3832
Proteinase K	Roth	7528.2
SDS	Biomol	04051.1
phenol/$CHCl_3$/isoamyl	Roth	A156.2

(*Continued on next page*)

Continued

REAGENT or RESOURCE	SOURCE	IDENTIFIER
RNAprotect reagent	QIAGEN	Cat# 76506
Superscript IV reverse transcriptase	Invitrogen	18090050
random hexamer primers	Invitrogen	Cat# SO142
dNTP mix	Thermo	R0192
RNAseOUT RNAase inhibitor	Invitrogen	Cat# 10777019
goTaq qPCR master mix	Promega	Cat# A6002
POPG: 1-palmitoyl-2-oleoyl-sn-glycero-3-phosphoglycerol	Avanti Polar Lipids	Cat# 840457
POPC: 1-palmitoyl-2-oleoyl-sn-glycero-3-phosphocholine	Avanti Polar Lipids	Cat# 850457
POPE: 1-palmitoyl-2-oleoyl-sn-glycero-3-phosphoethanolamine	Avanti Polar Lipids	Cat# 850757
POPS: 1-palmitoyl-2-oleoyl-sn-glycero-3-phosphoserine	Avanti Polar Lipids	Cat# 840035
LPG: 1,2-dioleoyl-sn-glycero-3-[phospho-rac-(3-lysyl(1-glycerol))]	Avanti Polar Lipids	Cat# 840521
Myristic acid	Sigma Aldrich	544-63-8
Pentadecanoic acid	Acros Organics	1002-84-2
Lauric acid	Sigma Aldrich	143-07-7
Palmitic acid	Sigma Aldrich	57-10-3
Palmitoleic acid	Sigma Aldrich	373-49-9
Stearic acid	Acros Organics	57-11-4
Linoleic acid	Sigma Aldrich	60-33-3
Diphenhydramine	Sigma-Aldrich	Cat# PHR1015
Polydimethylsiloxane (PDMS)	Biesterfeld	H047M3J042
Squalene Oil	Sigma-Aldrich	S3626
ClearSol CSV-2	Latitude	N/A
Xylose	Merck	Cat# W360600
Critical commercial assays		
BacLight Bacterial Viability Kit	Molecular Probes	Cat# L 7012
Roti Quant Universal	Roth	Cat# 0120.1
Monolith His-Tag Labelling Kit RED-tris-NTA 2nd Generation	NanoTemper	Cat# MO-L018
RNeasy mini Kit	QIAGEN	Cat# 74104
RNase-free DNase set	QIAGEN	Cat# 79254
Agilent RNA 6000 Nano reagents	Agilent	Cat# 5067-1511
Deposited data		
Genomes of Chlorotonil-resistant mutants to NCBI SRA	This manuscript	NCBI: PRJNA1150419
raw files and MaxQuant analysis to PRIDE (Full proteome)	This manuscript	ProteomeXchange: PXD051735
raw files and MaxQuant analysis to PRIDE (TPP)	This manuscript	ProteomeXchange: PXD051670
Cu-DHG Crystallographic data to CCDC	This manuscript	CCDC: 2376486
Al-DHG Crystallographic data to CCDC	This manuscript	CCDC: 2376487
Further crystallographic data to Zenodo	This manuscript	Zenodo: https://doi.org/10.5281/zenodo.14035926Zenodo: https://doi.org/10.5281/zenodo.13268606
Experimental models: Cell lines		
Hamster: CHO-K1	DSMZ	ACC 110
Human: HEK293	DSMZ	ACC 305

(*Continued on next page*)

Continued

REAGENT or RESOURCE	SOURCE	IDENTIFIER
Human: HepG2	DSMZ	ACC 180
Human: HCT-116	DSMZ	ACC 581
Experimental models: Organisms/strains		
SWISS mice, 6 weeks, male	Janvier Laboratories	N/A
Oligonucleotides		
metap_fwd: ggggacaagtttgtacaaaaaagcaggctttgagaatctttattttcagggcATGATTGTAAAAACAGAAGAAGAATTACAAG	Merck	Custom Synthesis
metap_rev: ggggaccactttgtacaagaaagctgggtgCTATTCTTCTTCAATCTTTGTCGTTAAAATC	Merck	Custom Synthesis
pETG41K (Gateway destination vector)	EMBL	https://grp-pepcore.embl-community.io/vectors/ecoli.html
farR fwd: GCATTGTCGAGTAGCTTGCTACAATTG	Sigma-Aldrich	Custom Synthesis
farR rev: GGAATGGATGATTAAGACGGTCACTG	Sigma-Aldrich	Custom Synthesis
farE fwd: GCGGTCATTGCATGGATAGTGATTG	Sigma-Aldrich	Custom Synthesis
farE rev: GTCTTCTGTAATGTTCGGTTGCACAATAC	Sigma-Aldrich	Custom Synthesis
16S fwd: GGCTCAACCTGGGAACTGC	Sigma-Aldrich	Custom Synthesis
16S rev: GCACCTGAGCGTCAGTCTTC	Sigma-Aldrich	Custom Synthesis
Software and algorithms		
GraphPad Prism 10.2 and 10.3	Dotmatics	https://www.graphpad.com
ITEM (v.5.2)	Olympus Soft Imaging Solutions	Only with instrument
Smart SEM (v5.05)	Zeiss	https://www.zeiss.com/microscopy/de/produkte/software/zeiss-smartsem.html#downloads
ICP/MS ChemStation B.04.00	Agilent	https://www.agilent.com/en/support/software-informatics/atomic-spectroscopy-data-systems/icp-ms-chemstation/g1834b-b0400-patch01
OpenLab CDS software version 2.6	Agilent	https://www.agilent.com/en/product/software-informatics/analytical-software-suite/chromatography-data-systems/openlab-cds
MaxQuant software	MPI Biochemistry Martinsried	https://www.maxquant.org/download_asset/maxquant/latest
Perseus software	MPI Biochemistry Martinsried	https://maxquant.net/perseus/
String DB	Global Biodata Coalition and ELIXIR	https://string-db.org
TPP R-package	Bioconductor	https://bioconductor.org/packages/release/bioc/html/TPP.html
Data Analyisis 6.1	Bruker Daltonics	Build: 331.2.0
HyStar 6.0	Bruker Daltonics	Version: 6.0.30.0
timsControl	Bruker Daltonics	Version: 5.1.8
ftmsControl 2.3.0	Bruker Daltonics	Build: 59

(*Continued on next page*)

Continued

REAGENT or RESOURCE	SOURCE	IDENTIFIER
R v4.1.2	R Core Team	https://cran.r-project.org/src/base/R-4/R-4.1.2.tar.gz
R Software drc v3.0-1 package	Ritz et al. 2015	N/A
Geneious Prime Version 2022	Dotmatics	https://www.geneious.com/
ZEN 3.7 software	Zeiss	https://www.zeiss.com/microscopy/de/produkte/software/zeiss-zen.html
ImageJ v. 1.53e	Schneider et al. 2012	https://imagej.net/ij/download.html
Other		
Noble agar	Difco Laboratories	0142-01
Diamond knife	Syntek Co., LTD	SYM3045 Ultra
Ni grids	Plano GmbH	G2300N
Cover slips (12 mm)	Menzel-Gläser	CB00120RA020
Gold-palladium target	Baltic Präparation	BP2229
Difco™ LB Broth, Miller (Luria-Bertani)	BD Becton Dickinson	Cat# 244620
BBL™ Mueller Hinton II Broth Cation Adjusted	BD Becton Dickinson	Cat# 212322
RPMI-1640 solution	Thermo Fisher Scientific Incorporated	11875093
RPMI-1640 powder	Thermo Fisher Scientific Incorporated	51800019
Magnetic Column Separation (LD Columns)	Miltenyibiotec	130-042-901
PES syringe filters	Roth	P821.1
HPLC column	Klaus Ziemer GmbH	Cat# 7.5841177
TLC silica plates	Merck	Cat#105554
Sep-Pak C18 columns	Waters	Cat# WAT054960
StrepTrap HP column	Cytiva	Cat# 28918779
Superdex 75pg	Cytiva	Cat# 28989333
HiTrap Desalting column	Cytiva	Cat# 17-1408-01
NanoTemper premium Capillaries	NanoTemper	MO-K025
LC-Pak Endfilter	Merck	Cat# LCPAK00A1
Hypersil GOLD 1.9 μm, 100 x 2.1 mm	Thermo Fisher	Cat# 25002-102130
UHPLC Filter Holder	Thermo Fisher	Cat# 27006
2.1 mm ID filter cart. 2 μm	Thermo Fisher	Cat# 22180
timsTOF fleX MALDI-2	Bruker Daltonics	N/A
Vanquish™ Flex UPLC-System	Thermo Fisher	N/A
InfiniteM200 PRO reader	TECAN	N/A
Microplate reader	CLARIOstar BMG Labtech	N/A
Monolith NT.115	NanoTemper	N/A
Agilent 2100 Bioanalyzer	Agilent	N/A
QuantStudio 5	Applied Biosystems	N/A
Patch clamp	HEKA Elektronik	N/A
Fluorescence Laser Microscopy	ZEISS	N/A

EXPERIMENTAL MODEL AND STUDY PARTICIPANT DETAILS

Microbe strains

S. aureus ATCC29213, *E. faecium* ATCC51559, *M. tuberculosis* H37Ra (ATCC25177) and *E. coli* ATCC25922 were purchased directly from ATCC. *E. coli* strains from Keio collection and their parent strain BW25113 were purchased from Horizon Discovery. *S. aureus* transposon mutants were retrieved from the Nebraska Transposon Library (USA300). Plasmodium strains were retrieved from BEI resources or kindly proved by Dr. David Fidock (Columbia University). All work was performed under biological safety level 2

or 3 using standard microbiological techniques. Quality control was performed on regular basis using MALDI-TOF (Ultraflex III, Bruker).

Cell lines

Cell lines were obtained from the German Collection of Microorganisms and Cell Cultures (DSMZ). The Chinese hamster ovary cell line CHO-K1 (DSMZ, female) was cultured in F12 medium. The human embryonic kidney cell line HEK293 (DSMZ, female) and the human hepatoma cell line Hep-G2 (DMSZ, male) were cultured in DMEM. The human colon carcinoma cell line HCT-116 (DSMZ, male) was cultured in McCoy medium. All media were supplemented with 10% heat-inactivated fetal bovine serum (FBS). From the used cell lines, only HEK are listed in the database of commonly misidentified cell lines maintained by ICLAC; the culture used in the present study was unambiguously identified by STR genotyping. According to DSMZ, the following authentication methods were used and revealed an authentic profile: mitochondrial Cytochrome C Oxidase Subunit 1 (COI) DNA barcoding for CHO-K1 (ACC-110) and standardized STR analysis for HCT-116 (ACC 581), Hep-G2 (ACC-180), and HEK293 (ACC-305).

Animal studies

All animal experiments were performed at a licensed CRO (SciVii labs GmbH, Saarbrücken, Germany). Six-week-old test naïve male mice of the SWISS strain from a licensed laboratory animal breeder (Janvier Laboratories) were used. The experiment was approved by the competent authority in accordance with the applicable EU and national animal welfare regulations (authorisation number 2.4.8-VG-01-2024-gv). The animals were kept in standardised type 2-L individually ventilated cages (IVC) from Tecniplast, in groups of 5. The animals were kept on aspen wood bedding and were given cardboard tubes, paper strips (sizzle nest) and gnawing wood-sticks. Food (standardised rodent diet, Sniff company) and water (tap water) were offered *ad libitum*. The animals were kept at the specified 20-24°C and a humidity of 45-65%, as well as a 12/12h automatic day-night rhythm. The test substance was dissolved in ClearSol (Latitude) and used after equivolume dilution with saline immediately prior application.

Blood samples were taken via the saphenous vein in accordance with the recommendations of the GV-Solas during the study and the final blood sample was taken via a cardiac puncture under terminal anaesthesia. Killing was performed via an overdose of anaesthetic (isoflurane) and subsequent cervical dislocation. The clinical chemistry data were collected using the Konelab 30i from Thermofisher.

METHOD DETAILS

Experimental compounds

All chlorotonil derivatives used in this study (see Figure S1), were produced by us and all characterisation data including NMR spectra have been published previously.[11,12]

Chlorotonil A: white powder. HRMS: C26H32Cl2O4 [M+H]+ calc.: 479.1756, found 479.1762. 1H NMR (500 MHz, CDCl3) δ 6.06 (ddd, J = 14.6, 11.5, 2.2 Hz, 1H), 5.89 (m, 1H), 5.75 (d, J = 10.1 Hz, 1H), 5.61 (m, 1H), 5.51 (dq, J = 11.4, 2.9 Hz, 2H), 5.39 (d, J = 5.2 Hz, 1H), 5.31 (dd, J = 10.3, 8.4 Hz, 1H), 4.55 (q, J = 7.0 Hz, 1H), 3.78 (m, 1H), 3.03 (dtt, J = 6.5, 4.1, 2.0 Hz, 1H), 2.80 (m, 1H), 2.36 (d, J = 9.3 Hz, 1H), 2.18 (m, 2H), 2.04 (dd, J = 16.8, 3.8 Hz, 1H), 1.77 (m, 1H), 1.66 (m, 3H), 1.55 (s, 3H), 1.33 (d, J = 6.7 Hz, 3H), 0.96 (d, J = 6.5 Hz, 3H), 0.84 (d, J = 7.0 Hz, 3H). 13C NMR (126 MHz, CDCl3) δ 196.9, 192.1, 168.0, 139.4, 133.2, 132.4, 130.4, 128.1, 125.6, 124.0, 123.7, 81.7, 70.4, 49.8, 47.2, 42.8, 38.4, 36.9, 33.5, 30.4, 30.3, 23.4, 21.1, 17.2, 15.8, 14.9.

ChB1-Epo2: white powder. HRMS: C26H34ClO5 [M+H]+ calc.: 461.2089, found 461.2094. 1H NMR (500 MHz, CDCl3) δ 16.12 (s, OH), 6.32 (m, 1H), 5.88 (t, J = 10.9 Hz 1H), 5.62 (m, 1H), 5.56 (m, 1H), 5.51 (m, 1H), 5.47 (m, 1H), 5.37 (t, J = 9.6 Hz, 1H), 4.38 (q, J = 6.9 Hz, 1H), 3.34 (dd, J = 12.3, 6.5 Hz, 1H), 3.03 (d, J = 5.3 Hz, 1H), 2.76 (m, 1H), 2.55 (m, 1H), 2.48 (m, 1H), 2.10 (m, 1H), 2.08 (m, 1H), 1.95 (td, J = 11.4, 6.0 Hz, 1H), 1.45 (d, J = 6.9 Hz, 3H), 1.41 (m, 1H), 1.35 (s, 3H), 1.34 (s, 3H), 0.93 (d, J = 6.5 Hz, 3H), 0.85 (d, J = 7.2 Hz, 3H). 13C NMR (126 MHz, CDCl3) δ 194.2, 187.8, 168.2, 138.7, 132.7, 131.7, 125.9, 124.4, 123.3, 109.2, 70.5, 64.7, 59.3, 45.6, 44.8, 42.1, 38.7, 36.0, 33.0, 28.5, 28.4, 23.0, 20.8, 16.8, 12.1, 10.2.

Dehalogenil: pale yellow powder. HRMS: C26H35O4 [M+H]+ calc.: 411.2529, found: 411.2536. 1H NMR (500 MHz, CDCl3) δ 15.56 (br s, OH), 6.44 (m, 1H), 5.98 (s, 1H), 5.86 (br t, J = 10.8 Hz, 1H), 5.74 (br d, J = 10.0 Hz, 1H), 5.57 (m, 1H), 5.55 (m, 1H), 5.51 (br dd, J = 6.1, 4.0 Hz, 1H), 5.39 (br t, J = 9.4 Hz, 1H), 5.35 (br dd, J = 3.1, 3.4 Hz, 1H), 3.52 (q, J = 6.8 Hz, 1H), 2.72 (dd, J = 12.0, 6.6 Hz, 1H), 2.63 (m, 1H), 2.62 (m, 1H), 2.58 (br d, J = 3.4 Hz, 1H), 2.13 (m, 1H), 2.09 (m, 1H), 2.01 (br dd, J = 16.9, 4.5 Hz, 1H), 1.74 (m, 1H), 1.67 (s, 3H), 1.41 (m, 3H), 1.34 (d, J = 6.8 Hz, 3H), 0.95 (d, J = 6.6 Hz, 3H), 0.77 (m, 3H). 13C NMR (126 MHz, CDCl3) δ 195.5, 190.1, 169.0, 139.1, 133.5, 132.5, 131.7, 128.2, 126.0, 124.4, 123.7, 102.4, 69.9, 49.0, 49.0, 46.0, 38.2, 35.4, 32.9, 31.1, 30.8, 23.5, 21.0, 16.5, 15.4, 11.9.

Susceptibility assays

Minimal inhibitory concentrations were determined using standard broth microdilution according to EUCAST guidelines (ISO20776-1:2019) in round-bottom 96-well plates. Regular quality control was performed using *Escherichia coli* ATCC25922 and appropriate reference antibiotics. MHBII medium was supplemented as stated in individual experiments using KCl or NaCl.

Growth analyses

Strains were grown overnight, split in fresh MHBII to reach final OD of 0.001, and then grown in regular round-bottom plates under constant orbital shaking at 37°C, absorbance was read every 15 minutes (Spark, Tecan). Compounds were either added directly from

the beginning (regular MIC set up) or added as indicated. Evaluation was performed using GraphPad Prism and its nonlinear fit for logistic growth to determine rate constant k and time to max growth rate. For lysis assay and K-rescue, cells were grown for an indicated amount of time prior addition of compound (final DMSO concentration 1%). Potassium was added as KCl (1/10 dilution from 4mM stock in MQ).

Time-kill-kinetics

An overnight culture was split 1/100 into fresh medium and grown to log phase prior dilution to $1x10^6$ or $1x10^8$ CFU/mL in pre-warmed MHBII (or MHBII supplemented with 400 mM KCl). Compounds were added in corresponding concentration (0.125-, 0.5-, 2-, 10-fold MIC) with a final DMSO concentration of 1%, while cells treated with DMSO only served as growth control. Samples were drawn at individual time points and diluted respectively in 50% FBS/PBS to avoid compound carry-over. Chlorotonils were found inactive in 50% FBS, as previously reported.[12] For K^+-TKC, cell were additionally washed once using saline solution. Plating was performed by spotting 10 μL of each dilution (10^2 CFU/mL limit of detection) on non-selective CASO followed by a viable cell count to determine colony-forming units (CFU). For K^+-TKC, LoD was 10 CFU/mL. If regrowth was observed, cells were tested for spontaneous resistance development.

Electron microscopy

Bacterial cells were fixed by adding both paraformaldehyde and glutaraldehyde at final concentrations of 5% respectively 2% to the culture medium. Transmission electron microscopy (TEM) sample preparation was done as described before except an additional uranyl acetate treatment during dehydration.[13] In brief, samples were washed twice with 0.1 M EM-HEPES buffer (HEPES 0.1 M, 0.09 M sucrose, 10 mM CaCl2, 10 mM MgCl2, pH 6.9) after fixation and treated with osmium tetroxide (1% in HEPES buffer) for 1 h at room temperature and followed by additional washing steps with HEPES buffer. Sample pellets were stabilized in 2% noble agar followed by dehydration in a graded series of ethanol (10, 30, 50, 70, and 90%) on ice, and two steps in 100% ethanol at room temperature, each step for 30 minutes. The 70% ethanol step was done with the addition of 2% uranyl acetate and incubation for 1 hour. Sample infiltration wit LR White (LRW) resin was subsequently done: LRW: EtOH -> 1:1, 2:1, 2x 100%) with approx. 8 hours for each step and followed by polymerization in small gelatin capsules at 50° C for 36-40 h. Ultrathin sections of approx. 50-70 nm thickness were cut with an Ultramicrotome Ultracut UC7 (Leica, Wetzlar, Germany) and counterstained with both, 4% aqueous uranyl acetate (3 min) and lead citrate (15 seconds). TEM image acquisition at calibrated magnifications was performed with a Libra 120 Plus (Zeiss, Oberkochen, Germany) using an acceleration voltage of 120 kV and the image analysis software ITEM (Olympus).

For scanning electron microscopy (SEM) sample preparation, bacteria were bound to 12 mm round cover slips with poly-L-lysine, fixed with 1% glutaraldehyde and washed twice with with TE-buffer, pH 7.0 (20 mM Tris/HCl, 1.0 mM EDTA). Afterwards, samples were dehydrated in graded series of acetone (10, 30, 50, 70, and 90%) on ice, and two steps in 100% acetone at room temperature, each step for 10 minutes followed by critical-point drying with liquid CO2 (CPD 300, Leica Microsystems, Wetzlar) and sputter coating with a gold-palladium film (SCD 500, Bal-Tec, Lichtenstein). SEM image acquisition was performed with a field-emission scanning-electron microscope Zeiss Merlin (Oberkochen, Germany) using both Everhart Thornley SE and the SE inlens detector and an acceleration voltage of 5 kV.

Propidium iodide stain

For membrane integrity assessment, we used the LIVE/DEAD BacLight bacterial viability kit (Molecular Probes), as previously described.[63] *S. aureus* ATCC29213 *was grown overnight at 37°C and 190 rpm and diluted 1:100 in cation-adjusted Mueller-Hinton broth and grown to exponential growth phase* (OD_{600} = 0.4-0.5) before being treated with different concentrations of DHG, along with 3% nisin or 1% DMSO as controls. Samples were withdrawn after indicated time points and stained with 3.34 μM Syto9 and 20 μM propidium iodide for 10 min in the dark. Cells were immobilized on 1% agarose and red and green fluorescence were acquired using the Nikon Eclipse Ti-E microscope (λ_{Ex} 305 nm, λ_{Em} 617 nm for PI; λ_{Ex} 483 nm, λ_{Em} 500 nm for Syto9). All statistical analyses were conducted for >300 cells from several independent experiments using the ImageJ software and the MicrobeJ plugin.[64]

FM5-95

Membrane fluidity was assess as previously described.[65] *B. subtilis* 168 *trpC2* growing exponentially in cation adjusted Mueller Hinton medium at 37°C (OD_{600} = 0.2-0.3) was treated with different concentrations of DHG, along with 1% DMSO as control. Samples were withdrawn after indicated time points, concentrated 1:2 and stained with 20 μg/mL N-(3-trimethylammoniumpropyl)-4-(6-(4-(diethylamino)phenyl)-hexatrienyl) pyridinium dibromide. Cells were immobilized on 1% agarose and analysed using a Nikon Eclipse Ti-E microscope (λ_{Ex} 515 nm, λ_{Em} 640 nm).

Induction of lia-lux cell wall stress response

B. subtilis luciferase reporter assays were conducted as previously described.[66] Briefly, *B. subtilis* 168 *sacA*:pCHlux101 ($P_{lial-lux}$)[67] was grown in Mueller Hinton Broth (MHB) containing 5 μg/mL chloramphenicol at 30°C to an OD_{600nm} of 0.5. Cells were added to 96-well white wall chimney plates containing serial diluted antibiotics (DHG 2 μg/mL, vancomycin 32 μg/mL) and luminescence measurements were performed at 30°C in a microplate reader Spark 10M (Tecan).

B. subtilis lacZ bioreporter agar assay

The agar assay was performed as described previously.[68] Overnight cultures of the bioreporter strains in LB containing 100 μg/ml spectinomycin were diluted to an OD_{600} = 0.05 and incubated at 37°C and 190 rpm until they reached an OD_{600} of 0.8 – 1.2. Cells were then concentrated 1:10 by centrifugation at 4700 rpm, 4 °C for 10 minutes. The soft agar (supplemented with 5 mM $MgCl_2$ and 150 μg/mL X-Gal, ThermoFisher Scientific) was inoculated with 3 x 10^7 CFU/ml. For the DNA (P_{yorB}) stress bioreporter LB soft agar was used (1% tryptone, 1% NaCl, 0.5% yeast extract, and 0.75% agar). The RNA stress (P_{yppS}) and the translation arrest (P_{bmrC}) bioreporter were tested in Belitzky minimal soft agar.[69] 0.4 μg of DHG were spotted on the solidified agar containing the different *B. subtilis* 1S34 bioreporter strains and incubated overnight at 30 °C (LB) or 37 °C (Belitzky minimal soft agar). The following Oxoid™ antibiotic discs (ThermoFisher Scientific) were used as positive controls: ciprofloxacin (5 μg), rifampicin (30 μg), chloramphenicol (10 μg), and vancomycin (30 μg).

UDP-Mur*NA*c pentapeptide accumulation

S. aureus HG001[70] was grown in 5 mL of MHB at 37°C to an OD_{600nm} of 0.6 and incubated with 130 μg/mL chloramphenicol for 15 min. DHG was added in different concentrations and incubated for another 30 min. LII_{PGN} -complexing vancomycin was used as positive control. Cells were harvested and extracted with boiling water, then the cell extract was centrifuged, and the supernatant lyophilized as previously published.[18] HPLC was performed on an Agilent 1260 Infinity II System (Agilent Technologies, Santa Clara, CA, USA) equipped with a VWD detector (260 nm). Separation was achieved on a MultoHigh Bio 300 – C_4 (4x125 mm, 5 μm) with a flow rate of 0.5 mL/min at 30°C, using a linear gradient of 0.01 M HCl for 3 min, which increased to 100% of 15% MeOH in 35 min, staying there for 5 min and returned to 0% in 2 min and kept there for 5 min before the following run.

MurG activity assay

The effect of Dehalogenil on MurG was investigated using heterologously expressed MurG-His_6 as previously described.[71] Activity was assayed in a final volume of 50 μl containing 2 mM Lipid I, 60 mM Tris-HCl pH 7.5, 5 mM MgCl2 and 0.5 % Triton X-100. The reaction was initiated by the addition of 2 μg MurG-His_6. After an incubation at 30°C for 30 min, the enzymatic reaction was stopped by the addition of 50 μl n-butanol / pyridinacetate (vol/vol 2:1; pH 4.2). After 3 min centrifugation at 10.000 g, the organic phase was analysed using thin-layer chromatography with chloroform/methanol/water/ammonia (88:48:10:1) as solvent. Conversion of Lipid I to Lipid II was visualized using PMA staining reagent A. Dehalogenil was added in different concentrations.

YbjG inhibition

Dephosphorylation of C_{55}PP was carried out using purified *S. aureus* YbjG-His_6 enzyme as previously described.[72] A total of 5 nmol of C_{55}PP was incubated with 3 μg of YbjG-His_6 in 20 mM Tris-HCl, at pH 7.5, 150 mM NaCl, and 0.8% Triton X-100 in 50 μL for 30 min at 37°C. The lipid fraction was purified using *n*-butanol/pyridine acetate, pH 4.2 (2:1; *v/v*). Analysis of the reaction was performed by HPLC using an Agilent 1260 Infinity II System (Agilent Technologies, Santa Clara, CA, USA) equipped with a VWD detector (210 nm). Separation was achieved on a MultiHigh Bio 300 – C_4 (4x125 mm, 5 μm) with a flow rate of 0.5 mL/min at 30°C, using a linear gradient of 3:1:1 (H_2O:MeOH:IPA) for 3 min, which increased to 100% of 0.25:1:1 (H_2O:MeOH:IPA) in 35 min, staying there for 5 min and returned to 0% in 2 min and kept there for 5 min before the following run. Both solvent mixtures were buffered with 10 mM H_3PO_4.

Microscale thermophoresis

Monolith His-Tag Labelling Kit RED-tris-NTA 2nd Generation (NanoTemper) was used for K_D determination with DHG and YbjG (25.4 kDa) following manufactures instructions. Briefly, YbjG concentration was adjusted in assay buffer (HEPES pH 7.5, 10% Glycerol, 1 mM MgCl2, 3.9 mM DDM, 1 mM imidazole) to 200 nM and labelled by RED-tris-NTA dye (100 nM) for 30 min in the dark. After centrifugation, this mixture was added to DHG dilution series (c_{start}=100 μM) and measured using Monolith NT.115 (NanoTemper) equipped with premium glass capillaries (NanoTemper, MO-K025). The experiment was repeated three times.

Membrane depolarisation

Membrane potential was assessed following previously published protocols.[33] Briefly, *S. aureus* ATCC29213 was grown overnight and diluted 1/100 in Luria-Bertani broth (LB) supplemented with 0.1% glucose (20% glucose stock in MQ, sterile filtered). The culture was grown to exponential phase (OD_{600} = 0.5-0.7), centrifuged at 4°C (4000x rpm for 5 min) and resuspended in 0.1% glucose in PBS (PBS-G) as assay medium to a final OD_{600} of 0.5. Cells were stained using 30 μM $DiOC_2(3)$ (3,3′-diethyloxacarbocyanine iodide, 3 mM stock in DMSO) and kept for 15 minutes in the dark at room temperature. Subsequently, 100 μL per well were transferred into a black 96-well plate (flat) and placed in a plate reader (Spark, Tecan). Fluorescence was read (λ_{Ex} 485 nm $\lambda_{Em,green}$: 530 nm; $\lambda_{Em,red}$: 630 nm) every minute. Baseline was recorded for two measurements, followed by a brief pause for compound addition before regular measurements were resumed until 30 minutes. Protonophore CCCP (5 μM, carbonyl cyanide 3-chlorophenylhydrazone) was used as positive control. For evaluation, red/green ratios were normalized against DMSO controls. Experiments were performed with two technical repeats per plate and three independent biological repeats displayed as average with standard deviation.

B. subtilis minD delocalization study

B. subtilis 1981 erm spc minD::ermC amyE::P xyl-gfp-minD,[73] a strain with a gfp-minD fusion under control of the Pxyl promotor, was grown in LB supplemented with 0.1 % w/v xylose at 30°C to an OD600 of 0.6.[66] For the experiments a no salt LB medium (not

including the 10 g/L NaCl) was prepared.[74] To prevent osmotic stress, the medium was substituted with 61.61 g/L glucose, which was autoclaved separately. Imaging was carried out within 2, 30, 60 and 90 min after addition of different concentration dehalogenil in relation to the MIC. The proton ionophore carbonyl cyanide m-chlorophenylhydrazone (CCCP, 100 μM) was used as positive control. Samples were immobilized on microscope slides covered with 1 % w/v agarose. Fluorescence microscopy was performed using a Zeiss Axio Observer Z1 microscope (Zeiss, Jena, Germany) equipped with TL LED light source, an Axiocam 820 mono camera and an Apotome 3. Images were acquired by optional sectioning with ZEN 3.7 software (Zeiss) and analysed and postprocessed using ImageJ v1.53e software.[21,75]

Potassium selective electrode

Potassium efflux was measured using a potassium-selective electrode (perfection, Mettler Toledo) with its respective meter (SevenDirect SD50), adapted from previously published methods.[76] The electrode was used according to manufacture instructions and calibrated prior each experiment using potassium standard (Mettler). Bacterial cells were grown to early stationary phase, washed once using 10 mM Tris/HCl (pH 7.4) supplemented with ion strength adjuster (ISA, Mettler), resuspended to OD30 in washing buffer, kept on ice and used within 30 minutes. 500 μL dense bacterial culture were mixed into 4.5 mL 10 mM Tris/HCl+ISA for each experiment. Compounds were added after 25s (baseline recording) and signal was recorded until stabilization was reached. For eukaryotic cells, $2x10^6$ cells/mL were resuspended in 5 mL low-potassium buffer (1/2PBS: 138.35 mM NaCl, 10.45 mM Na_2PO_4, 1.35 mM KCl, 0.9 mM KH_2PO_4) to stay in suitable range for the electrode (app. 100 mg/L [K^+]). After compound addition, cells were kept at room temperature with mild shaking for 30 minutes prior single point electrode measurements. For erythrocyte experiments, RPMI containing 2.5% haematocrit (human) was used, correspondingly treated, and centrifuged prior measurement of the supernatant. Experiments were performed in biological triplicates with mean and SD shown.

ICP-MS measurements

Inductively coupled plasma mass spectrometry (ICP-MS) was used to determine intracellular ion concentration of Na^+ and K^+, adapted from previously published methods.[13] Bacterial cells (50 mL) were grown to log phase (OD=0.5) and treated with indicated concentrations of DHG or DMSO for 30 minutes (n=3). 50 mL were then transferred to a fresh preweighed falcon and centrifuged at 4°C for 15 min at 4000g. The pellet was washed twice using 25 mL Tris/HCl buffer (10 mM, pH 7.4), and subsequently snap-frozen in liquid nitrogen. After lyophilisation, dry pellet mass was noted and used for normalization. Each cell pellet was digested at 90°C in a water bath for 30 minutes with the addition of 500 μL nitric acid (2 mol/L; trace metal grade). For complete digestion, samples were stored overnight at room temperature. On the next day, samples were mixed with 250 μL of an internal standard solution containing 10 ng/mL ^{9}Be and diluted to a final volume of 25 mL with water (ASTM type I). Calibration stock solutions were prepared to a concentration of 1.0 g/L from trace metal grade sodium chloride or potassium hydroxide (titrated with hydrochloric acid) in water, respectively, and calibration standards were diluted to contain equal masses of sodium and potassium in 40 mmol/L nitric acid, spiked with the internal standard. Prior to analysis, samples and calibration standards were filtrated through single-use PES syringe filters and transferred to measurement vials. To mitigate contamination, where appropriate, consumables used during sample preparation were cleaned with nitric acid, rinsed thoroughly with water and stored in sealed containers filled with water until usage.

Measurement of ^{9}Be, ^{23}Na and ^{39}K was conducted using a 7500ce ICP/MS instrument (Agilent, Waldbronn, Germany) equipped with a peristaltic sample pump, a Scott type spray chamber and a PFA μ-flow nebulizer. The plasma was operated at 1450 Watt. Measurement was performed for up to 25 cycles per sample for the three central points of each isotope in FullQuant mode, integrating signals over 1.0, 0.1 and 0.1 seconds per cycle for ^{9}Be, ^{23}Na and ^{39}K, respectively.

Using Agilent ChemStation software, signals of sodium and potassium were normalized against the signal of the internal standard, and the concentration of both elements in samples was determined using a linear fitting of the signals from the calibration samples. Elemental concentrations were expressed in relation to the dry weight of the cell pellets.

Maintenance of Plasmodium asexual stages

P. falciparum laboratory strains 3D7 (chloroquine-sensitive, provided by BEI resources, MRA-102), Dd2 (multidrug-resistant, provided by BEI resources, MRA-150), and Dd2_SJ557733 (SJ773355 resistant, provided by Dr. David Fidock, Columbia University, NY) were cultivated *in vitro* as previously described.[77,78] Briefly, the parasites were maintained in complete culture medium consisting of RPMI-1640 (Sigma-Aldrich) supplemented with 1M N-2-hydroxyethylpiperazine-N-2-ethane sulfonic acid (HEPES) solution (2.4% v/v) (Sigma-Aldrich), 200 mM L-glutamine (Gibco), 50 μg/ml gentamicin (Gibco), and 10% of AlbuMax II solution containing RPMI, hypoxanthine, NaHCO3, HEPES, D-Glucose and 50 g/l of AlbuMax II (0.5% wt/vol in culture medium) at 2.5% hematocrit. The cultures were kept at 5% CO2 and 5% O2, at 37°C, with a change of medium every two days. *P. falciparum* parasites were synchronized using magnetic column separation (MACS) before the assays.

Growth inhibition assays with asexual parasites

The assays were performed as described before[79,80]; briefly, the drugs were dissolved at 100 mM in DMSO or distilled water (chloroquine) and further diluted in complete medium to reach the desired concentration. Thereafter, drugs were distributed in a 3-fold serial dilution in 96-well plates. The highest concentration of the solvent (<0.1%) did not interfere with parasite growth. Synchronized ring-stage parasites were diluted to a parasitemia of 0.05% with O Rh+ erythrocytes in complete RPMI medium and seeded at a hematocrit of 1.5% in a total volume of 225 μL per well. Plates were subsequently incubated for 3 days at 5% CO2 and 5% O2 at 37°C

before the plates were frozen and thawed three times. Growth inhibition of *P. falciparum* was measured using an enzyme-linked immunosorbent assay (ELISA) for histidine-rich protein 2 (HRP2) using a microplate reader (CLARIOstar BMG Labtech) (excitation filter: 450 nm).

To assess the concentration of salts tolerated by *Plasmodium* parasites *in vitro*, a survival curve was performed with NaCl and KCl. Subsequently the highest ion concentration not influencing parasite growth (20 mM for both NaCl and KCl) was used to perform the growth inhibition assays , by simultaneously incubating the parasites with the constant concentration of salts (20 mM) and a serial dilution of the drugs.

All assays were performed at least three times in duplicates. Individual IC_{50} values were determined by nonlinear regression analysis of log concentration-response curves, using the drc v3.0-1 package of R v4.1.2.[81] Mean IC_{50} values and standard deviations (SDs) were calculated for each growth inhibition assay using Excel.

Full proteome analysis

Proteomics analyses of *S. aureus* ATCC29213 and the chlorotonil resistant mutants were performed as previously described with slight changes.[31] Briefly, cultures were inoculated from glycerol stocks into MHBII and grown overnight. The following day, the overnight culture was inoculated into fresh medium with DMSO (0.1%) or compound added (depending on the experiment) to an OD_{600} of 0.5. Cells were grown at 37°C, 200 rpm and the optical density was measured regularly. The samples were harvested (OD_{600} ~7) and washed with cold PBS (6000g, 4°C, 5 min) and reconstituted in 200 μL lysis buffer (PBS pH 7.4, 0.4% SDS, 1% Triton X-100). The cells were sonicated (10s, 30% intensity, Sonopuls HD 2070 ultrasonic rod, *Bandelin electronic GmbH*) and transferred into bead-mill lysis tubes filled with 0.1 mm zirconium beads. The cells were lysed at 6500 rpm for 3x30s using a precellys 24 bead beater (*peqlab*). The Lysate was centrifuged at 10.000g for 10 min, and the supernatant (180 μL) was transferred into a micro-centrifuge tube and centrifuged for 10 min at 21.000g. The supernatant (150 μL) was transferred into a new centrifuge tube. The protein concentrations of the samples were determined by BCA assay (Roti Quant, Roth), and all samples were adjusted to the same protein concentration using the lysis buffer. 80 μL of each sample was transferred into a 96-well PCR plate and the samples were alkylated with 10 mM TCEP and 20 mM iodoacetamide (IAA). 10 μL of a 1:1 mix of washed (3x H_2O) hydrophobic and hydrophilic carboxylate-coated magnetic beads (*Cytiva*) were added to each sample. To precipitate the proteins onto the beads, 135 μL ethanol were added to each sample. The plate was incubated for 10 minutes, 500 rpm. For each washing step, the plate was placed onto a 96-well magnet (*Dynamag*, *Invitrogen*) for 90s and the supernatant was carefully removed. The plate was then removed from the magnet and the next washing solution was added, followed by 1 minute shaking at 800 rpm. In this way, the samples were washed 3x with 180 μL 80% ethanol and once with 180 μL acetonitrile. The bead-bound proteins were digested in 50 μL 50 mM TEAB with 0.5 μg Trypsin (sequencing grade, *Promega*) overnight at 37°C in a tightly sealed plate and with a heated lid at 800 rpm. After the tryptic digest, the peptides were eluted from the beads, and the beads were washed with 50 μL of 1% formic acid and the resulting 100 μL were directly transferred into MS-vials without any desalting and 2.5 μL (250 ng) of each sample were measured on a timsTOF Pro in data-independent acquisition mode.

Peptides were measured and online-separated using an UltiMate 3000 nano HPLC system (*Dionex*) coupled to a *Bruker* timsTOF Pro mass spectrometer via a CaptiveSpray nano-electrospray ion source and *Sonation* column oven. Peptides were first loaded on the trap column (Acclaim PepMap 100 C18, 75 μm ID x 2 cm, 3 μm particle size, *Thermo Scientific*), washed with 0.1% formic acid in water for 7 min at 5 μL/min and subsequently transferred to the separation column (*IonOpticks* Aurora C_{18} column, 25 cm × 75 μm, 1.7 μm) and separated over a 36 min gradient from 5% to 17% B, then to 25% B over 18 min, then to 37% B over 6 min, followed by 10 min at 95% before re-equilibration and at a flow rate of 400 nL/min. The mobile phases A and B were 0.1% (*v/v*) formic acid in water and 0.1% (*v/v*) formic acid in acetonitrile, respectively. The timsTOF Pro was operated in data-independent dia-PASEF mode with the dual TIMS analyser operating at equal accumulation and ramp times of 100 ms each with a set $1/K_0$ ion mobility range from 0.60 to 1.60 V × s/cm^2 for MS1 scans. The dia-PASEF settings for fragmentation were set to a mass range of 400 to 1201 m/z and an ion mobility range of 0.60 to 1.43 V × s × cm^{-2}. Two ion mobility isolation windows were performed per dia-PASEF scan with 26 m/z window widths. A total of 32 isolation windows with 1 m/z overlaps to cover the mass range were used resulting in 16 dia-PASEF scans per MS1 scan and an estimated total cycle time of 1.80s (see Table). The collision energy was ramped linearly as a function of the mobility from 59 eV at $1/K_0$ = 1.3 V × s × cm^{-2} to 20 eV at $1/K_0$ = 0.85 V × s × cm^{-2}. TIMS elution voltages were calibrated linearly to obtain the reduced ion mobility coefficients ($1/K_0$) using three Agilent ESI-L Tuning Mix ions (*m/z* 622, 922 and 1,222) spiked on the CaptiveSpray Source inlet filter.

MS-data were analysed using DIA-NN (version 1.8.1)[82] using the library-free mode. The library was generated using the UniProt proteome for *S. aureus* USA300 (taxon identifier: 367830, downloaded on 07.06.2022, canonical). For the precursor ion generation, library generation and Deep-learning based spectra, RTs and IMs prediction were enabled. Trypsin/P with maximum 2 missed cleavages; protein N-terminal M excision on; Carbamidomethyl on C as fixed modification; no variable modification; peptide length from 7 to 30; precursor charge 2–4; precursor m/z from 300 to 1800; fragment m/z from 200 to 1800 for TIMS data. Precursor FDR was set to 0.01; Mass accuracy, MS1 accuracy and Scan window were all set to 0; isotopologues, MBR and Remove likely interferences were on; Neural network classifier in single-pass mode; protein inference at gene level; heuristic protein inference was enabled (–relaxed-prot-inf); quantification strategy was set to Robust LC (high precision); Cross-run normalisation was RT-dependent; Library generation smart profiling; Speed and Ram usage was set to optimal results. LFQ quantities were extracted from the protein groups (pg) results file and were further analysed with Perseus software (version 2.03.1).[83] LFQ intensities were log_2 transformed and protein groups with less than four valid values in at least one group were filtered out. Two-sample Students' t-test including permutation-based

multiple testing correction (FDR = 0.05) was performed for all relevant comparisons to calculate the fold-change and statistical relevance. Results table were exported and graphs prepared using *Graphpad* Prims 10.01.

Thermal proteome profiling

TPP was adapted as previously published.[84] *S. aureus* USA300 was inoculated into 2 separate culture tubes and grown overnight at 37°C, 200 rpm. All steps were performed in biological duplicates. The overnight cultures were inoculated into 20 mL medium and grown until stationary phase. The cells were harvested in falcon tubes and washed with cold PBS (6000g, 4°C, 5 min). The cells were reconstituted in PBS to a theoretical OD_{600} of 20/mL. Per replicate, 1.2 mL of the culture was transferred into two new microcentrifuge tubes and ChB1-Epo2 or DMSO were added (1:100, 1% DMSO final). The cells were incubated for 45 min at 37°C, 200 rpm and then each of the 4 samples was split into 10x 100 μL in 200 μL PCR tubes. The samples were placed into a preheated thermal cycler at the positions corresponding to the respective temperatures (42.3, 45.9, 49.2, 52.8, 56.4, 59.8, 62.6, 67.1, 71.1, 77.7°C). The samples were heated for 3 minutes, followed by an incubation at RT for another 3 minutes. Next, 100 μL of 2x Lysis buffer (PBS pH 7.4, 50 μg/mL Lysostaphin, 1.6% NP-40, 30 μg/mL DNAse I) and the cells were incubated at 37°C for 30 minutes. The samples were snap-frozen in liquid nitrogen and thawed at 25°C. This was repeated 4 times in total. 180 μL of each sample was transferred into a new Protein LoBind microcentrifuge tube and centrifuged (6000g, 4°C, 10 min) to remove cell debris. 160 μL of the supernatant were transferred into an ultracentrifuge tube (*Beckman Coulter*) and subjected to ultra-centrifugation (20 min, 100.000g, 4°C) to remove the aggregated proteins. The protein concentration of the supernatant of the first 2 temperature points was determined using the Roti®-Quant universal kit (Carl Roth) for BCA assay. All samples were adjusted to a total protein concentration of 65 μg in 100 μL based on the average of the first 2 temperature points, and the proteins were precipitated by adding a 5-fold excess of ice-cold LC-MS grade acetone and incubating overnight at -20°C. The following day the precipitated proteins were pelleted (21.000g, 20 min, 4°C) and the supernatant was aspirated. To remove residual impurities, the pellet was reconstituted in 500 μL ice cold methanol by sonication (10s, 10% intensity, Sonopuls HD 2070 ultrasonic rod, BANDELIN electronic GmBH & Co. KG) and pelleted again. The methanol was aspirated and the protein pellet was reconstituted in 200 μL X-buffer (7 M urea, 2 M thiourea in 20 mM HEPES buffer pH 7.5) and the proteins were reduced by the addition of 1 mM DTT (from 1 M stock in H_2O) and incubated under gentle mixing (25°C, 950 rpm, 45 min). To alkylate the reduced cysteines of the proteins, 5.5 mM iodoacetamide was added (550 mM stock in 50 mM in H_2O) and incubated for 30 minutes (25°C, 950 rpm). The alkylation reaction was quenched by adding 4 mM DTT (from 1 M stock in H_2O) and incubating for 30 minutes (25°C, 950 rpm). The proteins were pre-digested by adding LysC (2.5 μg/mL, 0.5 mg/mL stock, FUJIFILM Wako Chemical Corporation) and incubating for 3h (25°C, 950 rpm). After pre-digest, 600 μL 50 mM triethylammonium bicarbonate (TEAB) was added to each sample, followed by the addition of 1.3 μL of Trypsin (0.5 mg/ml stock, sequencing grade, modified; Promega) for overnight digest (37°C, 950 rpm). The following morning, the digest was quenched by adding 8 μL of formic acid (FA) and the peptides were desalted using Sep-Pak C_{18} 1 cc Vac cartridges (Waters) using the following procedure: Using gravity flow, the cartridges were first washed with 2 ml elution buffer (80% MeCN, 0.5% FA) followed by washing 3x with 1 mL 0.1% TFA. The samples were now loaded and washed 3x with 0.1% TFA and 1x with 0.5 mL 0.5% FA. The peptides were eluted from the cartridges with 2 x 250 μL elution buffer under gravity flow and once with 250 μL elution buffer under vacuum. The peptides were dried using a centrifugal vacuum concentrator and subsequently reconstituted in 7.5 μL TMT-labelling buffer (50 mM HEPES, 20% MeCN, pH 8.5) through repeated vortexing, sonication (bath) and centrifugation. For TMT-labelling, 5 μL of previously prepared TMT isobaric labels (TMT10plex™ isobaric Labels Reagent set 1x 0.8 mg, Thermo Fischer Scientific) were added (10 μg/μL stock concentration in anhydrous MeCN), vortexed, centrifuged and incubated for 1h (450 rpm, 25°C). The labelling reaction was quenched by the addition of hydroxylamine to a final concentration of 0.4%. To test whether the TMT labelling was successful, 187.5 μL of 0.1% FA were added to each sample, and 2 μL of each temperature point within a condition were combined, dried in a centrifugal vacuum concentrator, reconstituted in 1% FA, and the samples were measured using LC-MS/MS. After confirming complete TMT labelling, all temperature points within a condition were pooled (25 μg of protein based on initial protein concentration) and dried in a centrifugal vacuum concentrator. The combined samples were now fractionated. For this, the labelled peptides were reconstituted in 105 μL HILIC buffer A (95% MeCN, 0.1% TFA) by sonication and transferred to a LC-MS vial. The peptide fractionation was carried out using an UlitMate 3000 HPLC system (Dionex) equipped with an YMC-Pack PVA-Sil column (5 μm, 150 x 2.1 mm, 120 Å, YMC Europe GmbH). Gradient elution was carried out with 95% MeCN, 5% H_2O, 0.1% TFA (A) and 95% H_2O, 5% MeCN, 0.1% TFA (B). 100 μL of the sample was injected and separated using a 62.5 min gradient (7.5 min 0% B, 50 min to 30% B, 3.5 min to 50% B, 2.5 min to 100% B) at a flow rate of 0.2 mL/min, followed by a washing and equilibration step. During equilibration, an on-line UV detector at 215 nm was used to monitor peptide elution. Fractions were collected into a 96-well plate and then pooled into 5 greater fractions, which were dried in a centrifugal vacuum concentrator and subsequently reconstituted in 100 μL 1% FA by placing the tubes in a sonication bath for 10 min. The peptides were then filtered using freshly equilibrated (300 μL, 1% FA) 0.22 μM Ultrafree-MC® centrifugal filters (Merck, UFC30GVNB). The filtered samples were transferred into LC-MS vials. The experiment was conducted in duplicate.

TMT-labelled peptide samples were analyzed on an UltiMate 3000 nano HPLC system (Dionex) equipped with an Acclaim C_{18} PepMap100 (75 μm ID × 2 cm) trap column and a 25 cm Aurora Series emitter column (25 cm × 75 μm ID, 1.6 μm FSC C_{18}) (Ionoptics) separation column (column oven heated to 40°C) coupled to an Orbitrap Fusion (Thermo Fisher) in NSI-spray setting. For peptide separation, samples were loaded on the trap column and washed for 10 min with 0.1% TFA in ddH2O at a flow rate of 5 μL/min. Subsequently, peptides were transferred to the analytical column for peptide separation and separated using the following 120 min gradient (Buffer A: H2O + 0.1% FA; B: MeCN + 0.1% FA) with a flow rate of 300 nL/min.: in 10 min to 5% B, in 50 min from 5% to 22% and in 60 min from 22% to 35%. The separation gradient was followed by a column washing step using 90% B for 10 min

and subsequent column re-equilibration with 5 % B for 5 min. MS full scans were recorded at a resolution of 120.000 with the following parameters: Ion transfer tube temperature 275 °C, RF lens amplitude 60%, 375-1500 m/z scan range, automatic gain control (AGC) target of 2.0 x 10^5, 3 s cycle time and 20 ms maximal injection time. Peptides with a higher intensity than 5.0 x 10^3 and charge states between 2 and 7 were selected for fragmentation in the collisional-induced dissociation (CID) cell at 35 % collision energy and analysed in the ion trap using rapid scan rate. In the ion trap, the isolation window was set to 1.6 m/z, an AGC target of 1.0 x 10^4 and a maximal injection time of 100 ms. For MS3-based reporter ion quantification, the number of synchronous precursor selections (SPS) was set to 10 with an isolation window of 2.5 m/z. The selected precursors were fragmented using the higher-energy collisional dissociation (HCD) cell at 55% collision energy and analysed in the orbitrap at a resolution of 60.000 with the AGC target set to 2 x 10^5 and a maximal injection time of 118 ms.

MS raw data was analysed using MaxQuant software (version 1.6.17.0),[85] and peptides were searched against Uniprot database for *S. aureus* USA300 (taxon identifier: 367830, downloaded on 13.11.2020, canonical). Carbamidomethylation of cysteines was set as fixed modification, and oxidation of methionines and acetylation of N-termini were set as variable modifications. Trypsin was set as a proteolytic enzyme with a maximum of 2 missed cleavages. For the main search, precursor mass tolerance was set to 4.5 ppm and fragment mass tolerance to 0.5 Da. Fractions were assigned for each experiment. Group-specific parameters were set to "Reporter ion MS3 with 10plex TMT isobaric labels for N-terminal and lysine modification selected. The isotope correction factor was set for each TMT channel according to the data sheet of the TMT labels. Carbamidomethylation of cysteines was set as fixed modification, and oxidation of methionines and acetylation of N-termini were set as variable modifications. Trypsin was set as proteolytic enzyme with a maximum of 2 missed cleavages. For main search, precursor mass tolerance was set to 4.5 ppm and fragment mass tolerance to 0.5 Da. Second peptide identification was enabled, and false discovery rate (FDR) determination was carried out by applying a decoy database and thresholds were set to 1% FDR at peptide-spectrum match and at protein levels. The remaining parameters were used as default settings. Calculated corrected reporter ion intensities were normalized to the channel corresponding to the lowest temperature and were used to determine the melting curves of the proteins and the resulting thermal shifts (T_m). These were calculated using R (version 4.1.1) and the TPP package (version 3.20.1)[24] using the "analyzeTPPTR" function. Proteins that fulfilled all requirements[24,26] were considered to have a significant thermal shift. For visualization of the TPP output files, the data was filtered as follows: $R^2 > 0.8$ for all fitted curves, plateaus < 0.3 for DMSO curves, steepest slopes of melting curves < -0.06, difference in T_m between both DMSO replicates < 1.5°C. The resulting T_m shifts were visualized using GraphPad Prism 10.

Cloning and expression of *S. aureus* MetAP

The *map* gene was amplified from the extracted genomic DNA of *S. aureus* USA300 using PCR with the primers metap_fwd and metap_rev. The resulting PCR fragment was purified using a preparative agarose gel and subsequent DNA gel extraction. The cleaned PCR fragment was then cloned into pETG41K (EMBL) via pDONR207 (*Invitrogen*) using the Gateway BP and LR Clonase (*Invitrogen*) according to the standard manufacturer protocol. The plasmid was transformed into BL21 DE3 cells and grown on LB-kanamycin plates. Two colonies were picked, grown in LB-Kan and the plasmid extracted using a miniprep kit (*Macherey Nagel*). The plasmid was sequenced and a colony with the correct sequence was used for protein expression and purification. The MBP-TEV-*Sa*MetAP fusion protein was expressed solubly at 18°C overnight. 2 L of LB-Kan were inoculated (1:100) with BL21 DE3 pETG41K_*Sa*MetAP and grown to OD_{600} = 0.5. Protein expression was induced by adding IPTG to a final concentration of 0.5 mM. The next day, cells were harvested and washed with cold PBS. Cell pellets were reconstituted in lysis buffer (50 mM Hepes pH 7.5, 150 mM NaCl, 1 mM TCEP, 5% glycerol, 1 mM PMSF, small amount of DNASE) and lysed by sonication (7 min at 30%, 3 min at 60%, 7 min at 30% intensity, Sonopuls HD 2070 ultrasonic rod, *Bandelin electronic GmbH*). The lysate was cleared at 38.000 xg for 45 min and the supernatant was filtered through a 0.45 μm filter prior to purification using an Äkta Pure Protein Purification System (*Cytiva*). Due to the low binding capacity of the MBPTrap the purification was split into 14 runs (from 2 L harvested cells). Each time, 5 mL Lysate was loaded onto an equilibrated 5 mL MBPTrap column (*Cytiva*) at a flow-rate of 2 mL/min. The column was washed with 6 column-volumes (CV) buffer A (50 mM Hepes pH 7.4, 150 mM NaCl, 1 mM TCEP, 5% glycerol, 5 mM EDTA) at a flow-rate of 5 mL/min and eluted over 3 CVs with 100% buffer B (50 mM Hepes pH 7.4, 150 mM NaCl, 1 mM TCEP, 5 mM EDTA, 5% glycerol, 10 mM Maltose). The elution fractions were pooled (not concentrated) and the MBP-tag was removed by TEV cleavage using TEV-protease at a ratio of 1:20 at 4°C overnight (stirring). The following morning, the TEV-digest was monitored by IP-MS. Precipitated protein was removed by centrifugation. The supernatant was desalted using 2 combined 5 mL HiTrap Desalting column (*Cytiva*) into buffer C (50 mM Hepes pH 7.4, 150 mM NaCl, 1 mM TCEP, 5% glycerol) to remove EDTA. The His-MBP tag and uncleaved fusion protein was removed by loading the sample onto two connected 5 mL HisTrapHP columns (*Cytiva*) at a flow-rate of 5 mL/min. Cleaved *Sa*MetAP was eluted using 7.5% buffer D (50 mM Hepes pH 7.4, 150 mM NaCl, 1 mM TCEP, 5% glycerol, 500 mM imidazole). The bound HisMBP tag and fusion protein eluted only at 100% buffer D. The presence of cleaved *Sa*MetAP was confirmed by IP-MS and SDS-PAGE and the fractions were pooled and concentrated. The protein was then further purified by size-exclusion chromatography in buffer A using a Superdex 75pg (*Cytiva*) and eluted fractions corresponding to *Sa*MetAP were concentrated up to 10 mg/mL, snap-frozen in liquid nitrogen and stored at −80°C.

*Sa*MetAP activity assay

To measure the activity of *Sa*MetAP the protein was thawed on ice and diluted into assay buffer (50 mM Hepes, 150 mM NaCl, 0.1 mM TCEP) to a final concentration of 5 μM. The ideal metal concentration was determined to be a 3 to 5-fold excess of $CoCl_2$. The metal was added from a 100x stock (in ddH_2O) and the protein was incubated for 15 minutes at room temperature. Meanwhile, compounds

or DMSO were added to a plate from 100-fold stocks. 100 μL of pre-incubated cobalt-bound enzyme was added to each well. The plate was incubated at 35 °C for 15 minutes while measuring the absorption at 405 nM in a plate reader (*Tecan* F200 pro). The substrate was added using a Multipette® (*Eppendorf*). Here, 1 μL of 100 mM methionine-p-nitroanilide (MetpNA) was added for a final concentration of 1 mM. The absorbance was measured every minute for 3 hours. The release of cleaved para-nitroanilide was measured (405 nm) and the linear range was fitted by a linear regression fit and the slopes calculated using *GraphPad* Prism 10.01.

Crystal structure

A carbon-coated copper TEM grid was placed into an ethanol DHG solution in a 10 mL glass vial. A small hole was punched in the plastic lid of the vial to allow the ethanol to evaporate slowly. After two weeks, the solvent had evaporated, and green crystals up to 1 mm in size formed on the grid. The TEM grid was destroyed during this process. One of the crystals was selected under an optical microscope for crystallographic analysis. X-ray diffraction data were collected using a RIGAKU XtaLAB Synergy four-circle diffractometer at 100 K. The data were processed using CrysAlisPro 1.171.42.69a (Rigaku Oxford Diffraction, 2022). The structure was solved using SHELXT (Ver. 2018/2)[86] and refined with SHELXL-2019/2.[87]

Crystals of the aluminum DHG complex were obtained from a DHG ethanol solution with excess aluminum oxide powder. These crystals formed on the inner surface of a sealed 5 mL glass vial after several weeks of incubation. The crystals were harvested onto a nylon loop under an optical microscope, cryo-protected with 10% (v/v) (R,R)-2,3-butanediol, and flash-cooled in liquid nitrogen. Data collection was carried out at 100 K on beamline P11 of the PETRA III storage ring at the Deutsches Elektronen-Synchrotron (DESY, Hamburg, Germany). The maximum resolution obtained was limited to 0.66 Å by the detector edge at the closest possible distance to the sample, using the shortest reachable wavelength of 0.62 Å. HDF files were converted to CBF using the *eiger2cbf* tool (https://github.com/biochem-fan/eiger2cbf). The CBF files were then imported and processed in CrysAlisPro. The structure was solved using SHELXT (Ver. 2018/2) and refined using SHELXL-2019/2.[86,87]

Nanocrystals of the Co DHG complex suitable for electron diffraction measurements were obtained from an ethanol suspension of DHG and metallic cobalt after several weeks of incubation in a sealed 5 mL glass vial. A drop of the crystal suspension was placed onto a TEM carbon-coated copper grid, and the excess solvent was soaked up with filter paper. The grids were air-dried, clipped, and transferred into a Thermo Fischer GLACIOS TEM at room temperature. The grids were then cooled down to liquid nitrogen temperature within the TEM column. Data were collected using a Thermo Fischer EPU-D module in continuous rotation mode. The best seven SMV datasets were selected, processed, and merged using autoPROC.[88] The unit cell metrics and symmetry of the Co-DHG complex matched those of the Al-DHG complex, suggesting that the two crystals are isostructural. The data resolution was insufficient for structure determination by direct methods; therefore, molecular replacement, as implemented in Phaser[89] was applied. Analysis of the molecular geometry of the DHG ligand indicated that its conformation remained consistent in the Cu and Al complexes, so this ligand conformation was used as a search fragment for molecular replacement structure determination.

Resistance generation and sequencing

Chlorotonil-resistant mutants were produced by long-term exposure and adaptation (LEA) as previously described.[31] Briefly, cells were exposed to sub-inhibitory concentration antibiotic and grown for 24h at 37°C (180 rpm) in MHBII medium. For passaging, cells were split 1/100 in fresh selective medium with increasing concentration antibiotic. Once resistance was generated, Genomic DNA was extracted using a phenol-chloroform-isoamyl alcohol method. Cells were grown overnight and 3 mL were used for extraction. Cell lysis was performed in 10 mM Tris/HCl (pH 8.0) using 50 μg/mL lysostaphin (2 mg/mL in 20 mM NaAc pH 4.8) for 2h at 37°C (shaking). Then, cells were treated with RNAse (1 mg/mL) at 37°C for 0.5h followed by Proteinase K/SDS (2 mg/mL and 0.2%) for 1.5h at 55°C. The clear suspension was thoroughly mixed with equal amount of phenol/$CHCl_3$/isoamyl, followed by an incubation at room temperature for 10 min to allow for phase separation. After 10 minutes centrifugation (3500 g, RT), the upper aqueous phase was carefully transferred to a fresh tube (discard lower organic phase) and extraction steps were repeated until white interphase was gone. Then, 300 μL of final aqueous phase were transferred and mixed with equal amount of 3 M NaOAc solution (pH 4.8) prior to addition of 7 mL fresh absolute EtOH (-20°C). The DNA was precipitated overnight at -20°C and pelleted at 4000 rpm (5 min, 4°C). The pellet was washed once using 70°C EtOH (-20°C) and again centrifuged. After removal of the supernatant, the pellet was air dried and dissolved in 150 μL of 10 mM Tris/HCl (pH 8) for 1h at 55°C. Concentration, purity, and quality were evaluated using the nanodrop and agarose gel electrophoresis respectively.

The gDNA of wildtype and mutant samples were sent for Illumina MiSeq (2×300 bp reads, coverage >100) and analysed using Geneious Prime Version 2022. For short: paired reads were imported and mapped against the respective annotated reference genome retrieved from ATCC Genome Portal for *S. aureus* ATCC29213. After mapping, the consensus sequences were generated and aligned against the annotated reference genome (Progressive Mauve Algorithm) with a match seed weight of 15 and a minimum LCB score of 30,000. SNP calling was performed manually on the bases of both the original wildtype sample and the sequencing control grown for the entirety of the adaptation process.

RNA extraction and quantitative PCR

Wildtype and mutant strains were grown overnight, split 1/100 intro fresh medium and again grown to log phase. 500 μL were taken from each sample and mixed with 1 mL RNAprotect reagent (Qiagen). The sample was vortexed and incubated at room temperature for 5 minutes. Subsequently, centrifugation was performed at 5000g for 10 min, the supernatant was discarded and the pellet was stored at -80°C until subsequent RNA purification.

For RNA isolation, the pellet was mixed with 200 μL TE buffer (100 mM Tris, 1 mM EDTA, pH 8.0) containing 15 mg/mL lysozyme, 5 μg/mL lysostaphin and 20 μL proteinase K (Qiagen). The suspension was vortexed for 20s and incubated for 2h at 37°C in a heating block (1000 rpm). This was followed by a modified method of RNA isolation using the RNeasy mini Kit (Qiagen). For this, 700 μL Qiazol Lysis regent were added to the suspension, vortexed and incubated for 5 min at 30°C and 1000 rpm. Subsequently, the following phase separation was favoured by adding 140 μL of chloroform. The sample was vortexed for 15s, incubated for 5 min at room temperature and then centrifuged for 30 min at 21500g and 4°C. 500 μL of the upper aqueous phase were transferred to a new Eppendorf tube containing 750 μL of absolute ethanol and carefully inverted. Then 700 μL were loaded onto the column and centrifuged (17000g, 2 min, RT). The flow-through was discarded and the step was repeated with the remaining sample. Subsequently, 350 μL of RWT buffer prepared with 44 mL of isopropanol, was added and centrifuged (17000g, 2 min, RT). This is followed by DNase digestion using the RNase-free DNase set (Qiagen). For this, 80 μL (70 μL RDD buffer, 10 μL DNase stock solution) was added to the column and incubated at 30°C for 30 min. This was followed by one washing step with 350 μL RWT buffer and twice with 500 μL of RPE buffer. To remove the remaining solvents on the column, the sample was centrifuged dry at 21500g for 30 min (4°C), and then dried in a heating block at 50°C with the lid open for 30 min. In the final step, the RNA was eluted with 30 μL of RNase free water (17000g, 5 min, RT). Incubation at 70°C for 2 min was used to break up the secondary structure, followed by concentration and quality determination using the Nanodrop. RNA Integrity number (RIN) was determined using Agilent 2100 Bioanalyzer and its respective Agilent RNA 6000 Nano reagents.

RNA was converted to cDNA using Superscript IV reverse transcriptase (200 U/μL) in its standard 20 μL reaction set up with 50 μM random hexamer primers (1 μL), 10 μM dNTP mix (1 μL), 2 μg template RNA, 5xSSIV buffer (4 μL), 100 mM DTT (1 μL), RNAseOUT RNAase inhibitor (1 μL), and DEPC-treated water. Components were mixed and incubated at RT for 10 min, followed by 55°C for 10 min, and finally inactivated at 80°C for 10 min.

Primers were designed to quantify expression of *farR* and *farE*, as well as the endogenous control 16S rRNA using qPCR. For the reaction, we utilized goTaq qPCR master mix (Promega) containing all necessary components, and added respective forward and revers primers and cDNA template. Reaction was performed in technical triplicates and biological duplicates using a standard 40 cycle program with annealing temperature set to 60°C (QuantStudio 5, Applied Biosystems). Evaluation was done following the ΔΔCt method with 16S RNA and wildtype DNA as reference.

Lipid experiments

All lipids (POPG: 1-palmitoyl-2-oleoyl-sn-glycero-3-phosphoglycerol, 840457; POPC: 1-palmitoyl-2-oleoyl-sn-glycero-3-phosphocholine, 850457; POPE: 1-palmitoyl-2-oleoyl-sn-glycero-3-phosphoethanolamine, 850757; POPS: 1-palmitoyl-2-oleoyl-sn-glycero-3-phosphoserine, 840035; LPG: 1,2-dioleoyl-sn-glycero-3-[phospho-rac-(3-lysyl(1-glycerol))], 840521) have been purchased from Avanti Polar Lipids and stored at -20°C under nitrogen atmosphere. Fatty acids have been purchased from Sigma Aldrich (Merck). All stock solutions were prepared in methanol and kept at -80°C.

For native lipid mass spectrometry, protocol was adapted from published literature.[90] Briefly, a solution composed of 50 μM DHG and 500 μM of the respective phospholipid was prepared in methanol with 1% formic acid. Prior to the measurements, the mixture was incubated for 30 minutes at 4°C. The infusion into the Apollo II ESI-ion source of a timsTOF flex MALDI-2 (Bruker Daltonics) was performed using the integrated syringe pump at a 20 μL/min flow rate. Initial mass calibration of the instrument to an error lower than 2 ppm was performed using an ESI-L low-concentration tuning mix (G1969-85000, Agilent). The source temperature was set to 200°C with a nebulizer pressure of 1 bar and a dry gas flow of 5 L/min. Scans were acquired in the range from 150 to 2500 *m/z*. MS and MS/MS measurements were conducted with enabled trapped ion mobility spectrometry (TIMS) in a 1/K0 range of 0.55 to 1.90 V*s/cm^2. For all MS2 measurements, a static collision energy of 30 eV was used with an intensity threshold of 100 counts and a target Intensity of 4000 counts. The presence of the observed putative DHG-phospholipid complexes was validated via a DHG loss in the corresponding MS2-scans.

Due to the limited resolution on the previously described QTOF setup (approximately 70,000), the unambiguous validation of the POPG-DHG complex was not possible. Due to this limitation, the measurements were repeated on a SolariX XR (7T, Bruker Daltronics). The device was calibrated to a mass accuracy below 2 ppm and a mass resolution of above 1,000,000 in the relevant mass range using a 5 mM CsI solution. The source temperature was set to 180°C with a dry gas flow of 3 L/min and a nebulizer pressure of 0.8 bar. Infusion into the Apollo II ESI-ion source was achieved using the internal syringe pump at a flow rate of 120 μL/h. Spectra were recorded in a scan range from 150 to 4000 *m/z* with a data size of 16 M. MS/MS scans of the desired precursor were acquired after isolation of the precursor in a 5 *m/z* window and then achieving fragmentation using a collision RF amplitude of 1200 Vpp at a frequency of 2 MHz The collision energy was set to 20 eV.

Lipid membrane formation in microfluidics

The microfluidic chip was fabricated from Sylgard 184 using standard soft lithographic techniques bonded to a glass slide, as previously detailed.[91] The chip design featured two straight side-by-side channels with rectangular cross section forming an X-like geometry (Figure S6A). The two side-by-side channels are connected in their centre by a small orifice that is about 100 μm wide. For bilayer formation, the entire chip was initially filled with squalene oil containing dissolved POPG lipids at a concentration of 5 mg/mL. Subsequently, an aqueous solution containing 150 mM KCl and DMSO or DHG, was gently injected into both microfluidic channels using a pressure-controlled injection system. Upon injection of two aqueous fingers, their water-oil interfaces get decorated with a phospholipid monolayer. When those two monolayer meet at the orifice they form a bilayer.[91] Following bilayer formation, its

capacitance was measured by using a patch-clamp amplifier EPC 10 USB (Heka Electronics), equipped with two Ag/AgCl electrodes inserted to the inlets of the microfluidic channels applying 10 mV with a frequency of 10 kHz as an excitation signal. Using the size of the membrane in the equilibrated state being equal to the size of the orifice minus extension of the Plateau borders multiplied by the height of the chamber (100 μM), the specific capacitance could be calculated using following formula: Specific Capacitance C_s = capacitance / area.

Determination of dehalogenil blood concentrations

For the determination of dehalogenil concentrations in blood, 10 μL of blood sample of each time point were transferred into Eppendorf tubes equipped with glass inserts, followed by addition of 38 μL internal standard solution (10% methanol in acetonitrile containing 12.5 nM diphenhydramine) and 2 μL isopropanol. In parallel, a calibration was prepared by spiking different concentrations of dehalogenil in isopropanol into blood samples from vehicle-treated mice. Samples were centrifuged (15,000 rpm, 4°C, 20 min) and supernatants transferred into glass vials for analysis by HPLC-MS/MS (Vanquish Flex coupled to a TSQ Altis Plus, Thermo Fisher, Dreieich, Germany). HPLC conditions were as follows: eluent A: H2O + 0.1% formic acid, eluent B: acetonitrile + 0.1% formic acid, flow: 0.7 mL/min. The gradient was set to 10% B from 0 to 0.5 min, 10-90% B from 0.5 to 1.0 min, 90% B from 1.0 to 3.5 min and 10% B from 3.5 to 4.0 min. MS parameters: Spray voltage 4672 V (positive mode), vaporizer temperature 350°C, ion transfer tube temperature 380°C, sheath gas 30 (arb), auxiliary gas 10 (arb), ion sweep gas 2 (arb). Mass transitions for dehalogenil were as follows: precursor ion 411.22 m/z, with its products 355.08 m/z (collision energy = 22 V; RF lens = 66 V) and 393.08 m/z (collision energy = 11 V; RF lens = 66 V).

QUANTIFICATION AND STATISTICAL ANALYSIS

ImageJ was used to measure cell size of *S. aureus* cells and to assess septum fluorescence in MinD assay. GraphPad Prism Version 2022 and Perseus software (proteomics) was used for statistical analysis. GraphPad Nonlinear fit for logistic growth was used to determine rate constant k and time to max growth rate. Network correlations were evaluated using String Database analysis (https://string-db.org). Significance was calculated using Student's t test or multiple comparisons, as always indicated in figure legends. In the figures, * indicates $p < 0.05$, ** indicates $p < 0.01$, *** indicates $p < 0.001$, and **** indicates $p < 0.0001$. The number of biological replicates (n) is reported in the method part of STAR Methods details, figure legends, and description of results. The images presented are representative of three independent biological replicates. Data are presented as mean ± standard deviation (SD) or otherwise stated in figure legends.